THE JOURNAL OF PHYSICAL CHEMISTRY C

Article

pubs.acs.org/JPCC

Structural and Optical Properties of Mg and Cd Doped ZnO Nanoclusters

Samson B. Woodley,[†] Alexey A. Sokol,[‡] C. Richard A. Catlow,[‡] Abdullah A. Al-Sunaidi,[§] and Scott M. Woodley*[,‡]

[†]11 Gainsford Street, London SE1 2NE, United Kingdom

[‡]Kathleen Lonsdale Materials Chemistry, Department of Chemistry, University College London, 20 Gordon Street, London WC1H 0AJ, United Kingdom

[§]Physics Department, King Fahd University of Petroleum and Minerals, Dhahran 31261, Saudi Arabia

ABSTRACT: Global optimization and data-mining techniques have been used to generate the structures of Mg and Cd doped ZnO nanoclusters. The energy has been evaluated at three levels: interatomic potentials during the filtering stage, generalized gradient based (PBE) density functional theory during the refinement of structures, and hybrid (PBE0) density functional theory for the final electronic solutions used for the prediction of the cluster optical absorption spectra. The excitonic energies have been obtained using time-dependent density functional theory including asymptotic corrections. We considered three characteristic sizes of the host $(ZnO)_n$ cluster (n = 4, 6, 8) including all chemically sensible structural types as determined from their relative energy rankings and all possible dopant permutations. Thus, an exhaustive set of the solution structures could be assessed using configurational entropic contributions to the cluster free energy, which allowed us to draw a conclusion as to the oxide miscibility at this end of the size scale. With the exception of low temperature magnesium doped n = 4 and 6 nanoclusters, we find a continuous series of stable clusters. The former are predicted to disproportionate to the pure binary structures, which could be attributed to the competition between different structural types adopted by end members. The optical behavior of most stable clusters considered is contrary to the quantum confinement model.

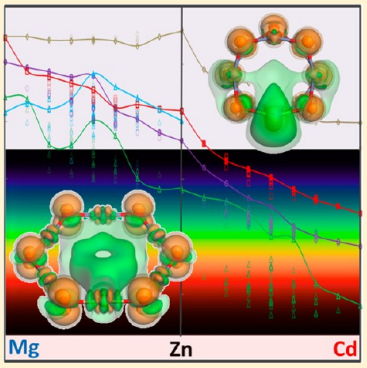

1. INTRODUCTION

The strong photoluminescence in UV and visible ranges coupled with robust mechanical and piezoelectric properties makes ZnO, a wide band gap, n-type semiconductor, a material of choice or potential candidate for applications in numerous electronic, optoelectronic, and light-emitting devices.[1] The room-temperature band gap energy of 3.37 eV for bulk ZnO (increasing to 3.44 eV at low temperatures) can be tuned to fit the intended applications by doping with suitable divalent elements without a great effect on charge carrier concentrations in ZnO, which might be undesirable. In particular, magnesium doping widens the band gap further into the UV range, causing a blue shift in the absorption spectra, while cadmium doping results in a red shift and targets devices that operate in the visible spectral range (1.7−3.2 eV). For a given stoichiometry, band gap broadening can also result from quantum confinement effects[2] that become pronounced as the size of the nanostructures is reduced and becomes comparable to the exciton Bohr radius (or rather diameter which is cited to be in the range of 26−58 Å for ZnO[3]); e.g., see report in ref 4. Moreover, this behavior is influenced by the environment of the nanomaterial as it can be stabilized in a matrix as a quantum dot, found in a solution, capped/passivated, or supported on a surface.[5,6]

There are clear constraints to such band gap engineering as structural changes and phase separation have been observed when the dopant concentration was increased beyond its solubility limit. Zn^{2+} and Mg^{2+} ions have similar sizes—Shannon radii of 0.60 and 0.57 Å in four-coordinated and 0.74 and 0.72 Å in six-coordinated environments[7]—whereas Cd^{2+} is a larger cation with a radius of 0.78 and 0.95 Å. Curiously, Zn seems to be of just the right size for its oxide to form a tetracoordinated wurtzite structure,[8] whereas oxides of both the smaller and the bigger ions, MgO and CdO, adopt the hexacoordinated rock-salt phase; however, this will also be influenced by the character of chemical bonding determined by the cation electronegativity.

In synthetic $Mg_xZn_{1-x}O$ thin film alloys, segregation of MgO has been observed beyond x = 0.33, which limits the maximum value of the band gap to 3.99 eV.[9] Nanoclusters of ZnO doped with 17% Mg also show an increase in the band gap to 4.0 eV,[10,11] which should be contrasted with the later report of a 0.5 eV blue shift on ∼7.5% Mg doping.[12] These observations prove to be morphology dependent: an increase in the band gap up to about 3.7 eV has been observed[13] in ZnO hexagonal nanorods also doped with 17% Mg. Pure and Mg doped (at 14%) ZnO nanoparticles, obtained by flame spray synthesis, show a difference in the band gap of only 0.2 eV.[14] Turning to Cd doping, a transition from the wurtzite to a rock-salt phase was observed at x = 0.7 in $Cd_xZn_{1-x}O$ films.[15] In contrast, a maximum

Received: August 23, 2013
Revised: November 1, 2013
Published: December 13, 2013

   dx.doi.org/10.1021/jp4084635 | J. Phys. Chem. C 2013, 117, 27127−27145

Cd content of about 17% has been reported for ZnO nanorods.[16] For ZnO nanoparticles, the band gap is reduced by about 0.4−0.5 eV on doping with 10% Cd[17] and 0.35 eV with 9% Cd,[18] whereas a decrease in the band gap of about 0.15 eV was observed[19] in ZnO nanorods doped with 5.5% Cd. A decrease of ∼0.08 eV was reported for 2% Cd doped nanostructures synthesized by a high-pressure solution route.[20] Tentative optical characterization of smaller particles or nanoclusters has also been reported, which, however, gives very high values of the absorption edge, possibly due to an interaction with matrix environment.[21] We note that doping ZnO nanostructures with Mg and Cd should be considered in the context of other significant efforts applied to synthesis of nanostructures with desired magnetic or electrical conducting or catalytic properties, which make use of alkali, transition, lanthanide, or group 13 metals in the cationic sublattice or group 15 in the anionic sublattice; for example, see refs 14 and 22−31.

Previous computational work on the characterization of optical properties of zinc oxide nanoparticles focused mainly on the pure material.[32−37] For a review of structure prediction of ZnO nanoclusters, we refer the reader to our earlier perspective and the references cited therein.[6] Similar nanoclusters are found for MgO; see for example ref 38 which contains the most recent structure exploration on the DFT energy landscape for up to 16 binary units. Nanoclusters of CdO have received less attention; structures for 1−8 binary units are reported in ref 39. ZnO clusters doped with other transition metals have been studied.[40−48] Ovsiannikova[48] incorporated Cd on cationic sites on the hexagonal faces of high symmetry bubble structures (e.g., $Zn_{24}Cd_{12}O_{36}$ bubble), whereas typically the focus of the other simulations was the clarification of the magnetic interactions at the nanoscale rather than optical response. Only one and two substitutions per cluster were investigated, and only Chen and Wang[45] considered different cation permutations. Dopants in simulations of ZnO clusters also include main group trivalent metals,[40] carbon,[49−52] nitrogen,[53,54] and sulfur.[52,55,56] Effects of the environment, including ligands or a surrounding matrix for example, have also been investigated.[57−60] However, none of these studies has addressed the problem of the effect of structural diversity on the calculated optical response by the material on doping. We will show that the interplay between the structure type (morphology) and dopant positions in the host determines the behavior of the cluster exposed to radiation in the UV/vis range.

In our previous work we have addressed the problem of structure diversity in pure binary compounds,[61−70] where the challenge is broken down into constrained searches for lowest energy configurations, and the essential unknown variables are the atomic coordinates for a predescribed composition (stoichiometry and size). Typically, the electronic degrees of freedom are also constrained during the search (e.g., assuming only one ionic type of bonding within each cluster). Thus, an energy landscape for each composition is defined, and local minima are determined by employing global optimization techniques. The resulting structures are then used to predict physical or chemical properties of the particles. On doping, we encounter a further complication in that both the extent of doping and the dopant arrangement within each host (parent) structure are not known. Each of the variables considered will affect the absorption and luminescence among other properties. Only the lowest energy configuration of the pure compound is usually doped,[71] but as doping progresses the host structure type may change. To catch this effect, the lowest energy configurations of both pure end members of the solution should be doped exhaustively (data mining). But this strategy is also vulnerable as the mixed compound could adopt a different structural type—we will find that being the case for $(Zn_xMg_{x-1}O)_8$. Therefore, it is important to consider a number of low-energy minima or to perform a direct global search on the energy landscape of the ternary compound (cf. ref 72). With the extra degrees of freedom, the latter of course quickly becomes intractable for larger sized particles. This problem is analogous to that of finding the lowest energy configurations of nanoalloy clusters where different permutations of the same structural type are referred to as *homotops*.[73] Moreover, as the energy differences we find are typically smaller than thermal energies, we have carried out an exhaustive survey of all possible homotops and all low-energy configurations that could be identified using a wide range of global optimization approaches applied to ZnO. Furthermore, the synthesis and experimental characterization of subnanosized particles, or clusters, remain in the realm of development and are still imprecise. Hence, our approach will provide a useful database as a reference point for comparison with experiment and benchmarking of alternative stochastic studies. Indeed, for pure binary compounds there has been success in identifying particular global minima or a number of local minima, rather than a larger range of local minima structures.[38,74]

In this work, we investigate the optical properties of $(Zn_{1-x}A_xO)_n$ nanoclusters as a function of size, n = 4, 6, and 8, and concentration of the dopant, A, which is either Mg or Cd. The first task is to find the atomic structure of these nanoclusters, where we need to reduce the computational cost required to search the DFT energy landscape for stable and low-energy metastable structures for each chosen value of x, n, and A. We therefore initially employ an atomistic model (using interatomic potentials, IP) and filter out approximate atomic configurations that can be readily refined at the DFT (electronic structure) level. This multistage approach, a global optimization of atomic structure for low-energy IP minima followed by refinement of atomic structures using standard local optimization techniques to obtain DFT energy minima structures, has already proved successful.[6,65,75] We have chosen two global optimization techniques: the first is an evolutionary algorithm,[65] which is initially applied to searching the IP energy landscapes for $(ZnO)_4$, $(ZnO)_6$, $(ZnO)_8$, $(MgO)_4$, $(MgO)_6$, and $(MgO)_8$, and the second is an exhaustive data-mining exercise of the lowest energy configurations found in the former search to obtain approximate atomic configurations for $(Zn_{1-x}A_xO)_n$ nanoclusters. Results for $(Zn_{1-x}Mg_xO)_n$ nanoclusters are presented in section 2. DFT energies for the refined $(Zn_{1-x}A_xO)_n$ nanoclusters are then reported for both Mg and Cd dopants in section 3 and their optical spectra in section 4.

2. FILTERING OUT PLAUSIBLE LOW-ENERGY STRUCTURES

Using an evolutionary algorithm[65] to search for local minima (LM) on six independent energy landscapes, the stable and low-energy metastable atomic structures for magnesium and zinc binary oxide clusters, $(ZnO)_n$ and $(MgO)_n$, were generated for sizes n = 4, 6, and 8. In this work, the unique minimum-energy structures found are referred to as structural types. At this initial stage, a rigid ion model is employed using species-dependent two-body interatomic potentials acting between the point charges that represent the ions. The functional form (a combination of polynomials, Buckingham, and Lennard-Jones

terms) and parameters of the interatomic potentials used for MgO are defined in Table 1; those for ZnO are taken from ref 76.

Table 1. Parameters for the Interatomic Potential for MgO: $A_{ij}\exp(-r_{ij}/\rho_{ij}) + B_{ij}/r_{ij}^{12} - C_{ij}/r_{ij}^{6} + Dq_iq_j/r_{ij}^{a}$

i	j	A_{ij} (eV)	ρ_{ij} (Å)	B_{ij} (eV·Å^{12})	C_{ij} (eV·Å^{6})	q_i
Mg	O	888.998	0.318 13	1.0	0.0	2.0
O	O	23674.698	0.226 40	1.0	33.4765	−2.0

[a] r_{ij} is the distance between ions and D = 14.399 758 4 eV•Å.

Although the structural types found for magnesium oxide were also found for zinc oxide, with these interatomic potentials (IP energy) there are more structural types for the latter.

After completing the global search for the two end members, we then generated all the unique zinc−magnesium cation permutations for a range of low-energy structural types found. These $Zn_{n-m}Mg_mO_n$ (n = 4, 6, and 8, m = 1 to n − 1) nanoclusters were then relaxed. The lowest energy clusters including the structural types, or end members (m = 0 and n), are shown in Figure 1.

For n = 4, the same three structural types with the same ranking, as determined by the IP energy of formation, were found for the end members, $(ZnO)_4$ and $(MgO)_4$; an octagonal ring is the global minimum (GM, or LM1) structural type, then a cuboid (LM2), followed by a configuration composed of folded and merged hexagonal rings (chimera, or LM3); see topmost panel of Figure 1. Whereas the ring and cuboid only have one unique site, LM3 has two. Since one of these sites resembles that found in the ring (two-coordinated) and the other in the cuboid (three-coordinated), we will refer to LM3 as a chimera. For the mixed oxides, the cation order has a less significant effect on the ranking than the structural type; comparing configurations with equivalent composition, the formation of a ring configuration is always more favorable than the cuboid, which in turn is more favorable than the chimera configurations. There are two unique chimera configurations for members m = 1−3, two unique ring configurations for $Zn_2Mg_2O_4$, and one otherwise. As a dopant, the magnesium (in the zinc-rich m = 1 cluster) and zinc (in the

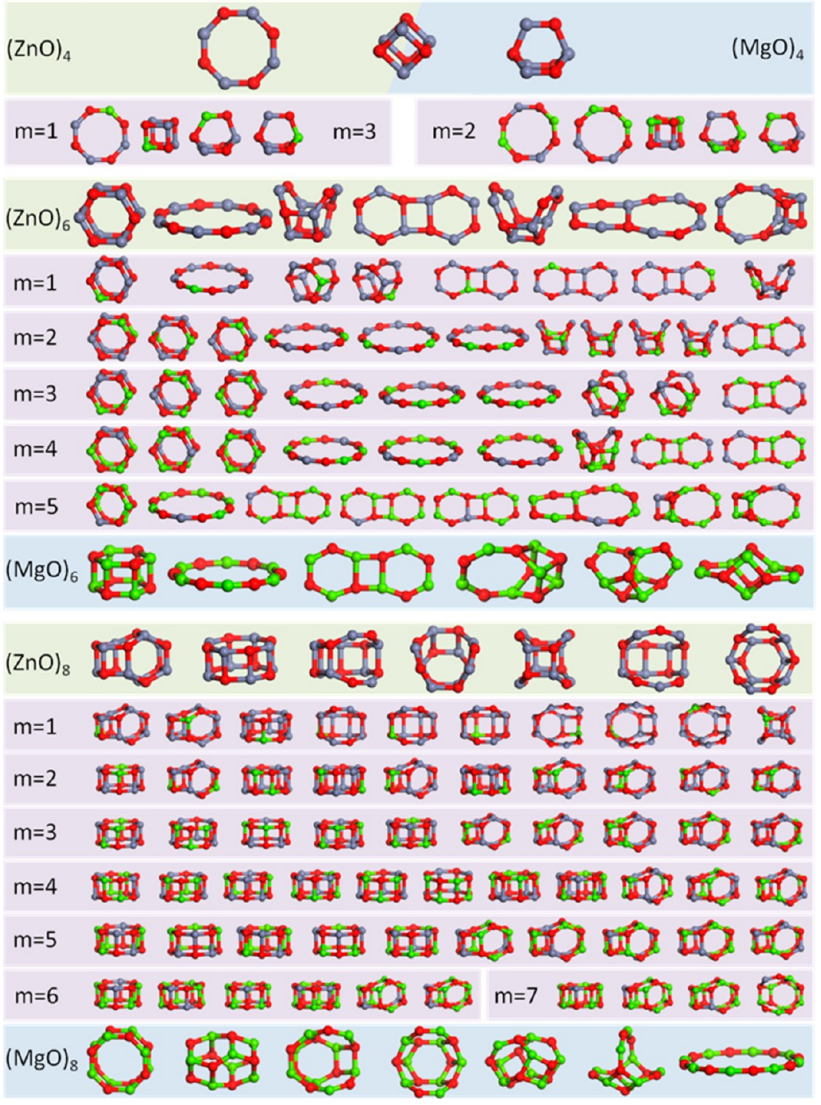

Figure 1. Stable and metastable $Zn_{n-m}Mg_mO_n$ nanocluster IP configurations for n = 4, 6, and 8 and m = 0 to n. In each panel the clusters are arranged by rank, with the IP global minimum of each compound on left-hand side. Gray, green, and red spheres indicate zinc, magnesium, and oxygen atoms, and for the n = 4 clusters complete sets of zinc and magnesium atoms are interchangeable (colors for zinc and magnesium atoms reversed).

dx.doi.org/10.1021/jp4084635 | J. Phys. Chem. C 2013, 117, 27127−27145

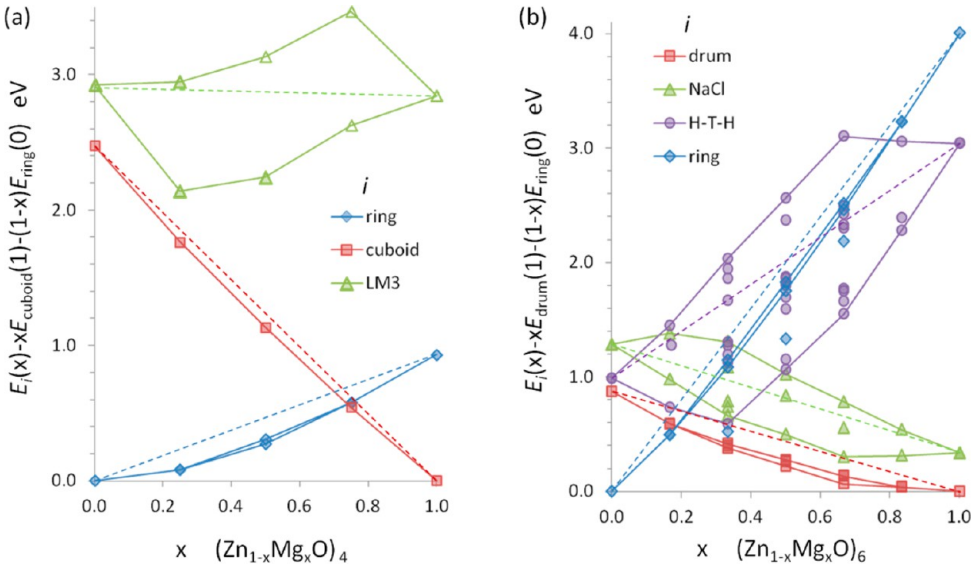

Figure 2. DFT solution energies, $\Delta E_i(x)$, for clusters of (a) $(Zn_{1-x}Mg_xO)_4$ and (b) $(Zn_{1-x}Mg_xO)_6$. The solid lines connect the highest and lowest energy configurations for each structural type; the broken lines represent the arithmetic mean energy of mixing end members (solution energy of zero for that structural type); and the four unfilled triangles represent unstable configurations (constrained during relaxation to either C_{3v} or pseudo-C_{3v}).

magnesium-rich m = 3 cluster) tend to occupy the lower, two-coordinated sites of the chimera. For clusters with equal content of magnesium and zinc (m = 2), one of the two magnesium cations prefers to occupy the three-coordinated site, whereas in the octagonal ring structure, like cations are more stable in opposite corners of the polygon (cation type alternate around the ring).

For all compositions (m = 0−6) of cluster size n = 6, the hexagonal prism (drum) is the most stable structural type; the energies of formation for other possible cluster types, with the same value of n and m, are higher than those for the drum. In each panel of Figure 1, clusters of the same structural type are grouped together and therefore have a continuous set of ranks; the rank of each n = 6 structural type investigated does not depend of the cation order. For each value of m, the dodecagonal ring is the second lowest energy n = 6 structure type. After the drum and ring, a number of the structural types found for $(ZnO)_6$ are unstable for $(MgO)_6$, including two open drums—the drum with either two or three elongated bonds connecting the two hexagonal rings—and an edge-sharing hexagon−octagon 2D structural type. For composition m = 5, five of the six possible unique configurations for the latter 2D structural type are unstable. Moreover, an open drum is also unstable if there are not enough zinc cations to occupy all two-coordinated sites. A comparison of the metastable open-drum structures (including the planar hexagon−tetragon−hexagon cluster) reveals that lower energies are obtained if magnesium atoms occupy higher coordinated cation sites, whereas zinc atoms occupy the two-coordinated cation sites. For the closed-drum structural type, there is only one unique cation site and likewise for the ring. The most stable ordering of dopants in the latter maximizes the interatomic distances between dopants, whereas in the double ring, or drum, a more stable configuration is obtained if the like cations preferred to occupy the same tetragonal ring(s). For the three unique m = 3 configurations, the greatest energy cost is predicted for segregation of magnesium and zinc cations into different hexagonal rings.

For $Zn_{8-m}Mg_mO_8$ (m = 1−7) nanoclusters we find similar trends in the cation ordering: the IP energy of formation is reduced if the coordination of Mg cations is increased, and in the drum structural type (which is now an octagonal prism) lower energies are found if the interatomic distances between like cations are maximized within each of the two larger (octagonal) rings and minimized between them (thus, occupying the same tetragonal ring(s)). Interestingly, the IP rank of the n = 8 structural types *is* dependent on m; the drum is the GM (or GM set) for m = 2−8, whereas for m = 0−1 it is a bubble formed from four hexagonal and six tetragonal faces.[65] As with smaller sized clusters, the energy difference between the lower energy structural types is larger than that which can typically be achieved by reordering the cations within one structural type. In Figure 1, there are only two examples where the ranks of different structural types overlap—the drums and bubbles for $Zn_6Mg_2O_8$—and the lowest energy configuration for the fifth structural type for Zn_7MgO_8 (last cluster in m = 1 panel) has a lower energy than five of the eight unique metastable configurations for the fourth structural type. Again, more LM are found for clusters of zinc oxide than magnesium oxide; the open-drum configurations LM3, LM5, and LM6 in the panel for $(ZnO)_8$ are not found for magnesium oxide (likewise, an increasing ratio of unique configurations are unstable as the content of Mg grows). The LM4 and LM7 structural types for $(ZnO)_8$ are also metastable $(MgO)_8$ clusters even though they, and the other higher energy clusters shown for $(MgO)_8$, contain two-coordinated cation sites. Note that all results reported so far are obtained using a rigid ion model (interatomic potentials acting between +2|e| and −2|e| point charges, representing the cation and anion, respectively).

3. DFT ENERGETICS AS A FUNCTION OF NANOCLUSTER STRUCTURE TYPE AND DOPANT CONCENTRATION

The nanoclusters were all refined using a density functional approach as implemented in DMOL[377,78] using the generalized gradient approximation in the PBE form,[79] a double numerical with polarization basis set and auxiliary charge density expanded up to octupoles. We define the energy of each nanocluster as E_i^j, where the label i refers to the structural type and j is used to

dx.doi.org/10.1021/jp4084635 | J. Phys. Chem. C 2013, 117, 27127−27145

distinguish different homotops (cation permutations) and is omitted for binary compounds as there is only one homotop. To characterize the relative stability of clusters of different stoichiometry, we will employ solution energies (heat of mixing):[80]

$$\Delta E_i^j(x) = E_i^j(x) - xE_r(1) - \{1 - x\}E_s(0) \quad (1)$$

where x is the stoichiometric ratio of the cluster and $E_r(1)$ and $E_s(0)$ are the global minimum energies for the end members. We note the use of r and s to indicate the structural type as the global minimum may change with x, so that the last two terms give an arithmetic mean of the binary global minima, and nanoclusters are constrained in size; i.e., we consider n = 4, 6, and 8 structures as independent ensembles. If ΔE is positive, then such an ensemble of nanoclusters is predicted to disproportionate to pure binary clusters in the low-temperature thermodynamic limit. We are also interested in the ensemble composed of the subset of clusters for each structural type, in which case we set $r = s = i$ in eq 1.

The solution energies for $(Zn_{1-x}Mg_xO)_4$, or $Zn_{4-m}Mg_mO_4$ nanoclusters are shown in Figure 2a. As predicted earlier for IP-based energies, the chimera structural type is less favorable than the ring and cuboid. Likewise, considering the cation order within the rings, the same ranking is found; the −O−Mg−O−Zn−O−Mg−O−Zn− ring is the lowest $Zn_2Mg_2O_4$ (m = 2, or x = 0.5 in Figure 2) IP and DFT energy configuration. For clusters with a high concentration of zinc, there is a good agreement between IP and DFT rankings, whereas for magnesium rich clusters (m = 3 and 4, or x = 0.75 and 1.0 in Figure 2) a cuboid (rock-salt fragment), rather than the ring, is predicted to be the stable configuration. IP results for chimera configurations predict that the magnesium cation prefer a two-coordinated (ring-like) site for Zn_3MgO_4 and the higher, three-coordinated (cuboid-like) site otherwise (m > 1). Given the change in the predicted ground state for $(MgO)_4$, it is not surprising that the rank for the two Zn_3MgO_4 chimera clusters also changes. Moreover, if more than one of the three two-coordinated sites is occupied by a magnesium cation, the DFT results predict that the chimera clusters with higher magnesium concentrations are unstable and will relax to the cuboid structure unless symmetry constrained; i.e., one m = 2, both m = 3, and the m = 4 configurations are unstable. Thus, our DFT results indicate a more consistent tendency for magnesium/zinc to occupy higher/lower coordinated sites, which is reflected in the predicted global minima (rock-salt/ring structural types are composed of three/two-coordinated sites) and in the energy ordering of Mg doped chimera configurations (that are composed of both three- and two-coordinated sites). To obtain the cuboid as the stable configuration for $(MgO)_4$, without resorting to DFT, one could implement either a partial charge model[81] or the shell model.[65] With similar energies, both the cuboid and ring structural types are likely to be adopted at room temperature for $ZnMg_3O_4$ (x = 0.75 in Figure 2), whereas rings with a random cation distribution are predicted for $Zn_2Mg_2O_4$ (x = 0.5 in Figure 2). Cation ordering only has a significant effect on the chimera: for the mixed cation clusters of the ring and cuboid, all cation distributions favor a solution rather than segregation into pure zinc and magnesium oxide clusters of the same configuration type (data points below their respective broken line in Figure 2), whereas a unique cation distribution is favored for a mixed chimera.

The relative DFT solution energies for four n = 6 structural types—three based on the lowest IP energy LM for $(MgO)_6$ and one a cuboid cut from bulk MgO—are shown in Figure 2b. Note that both LM3 and LM5 for $(ZnO)_6$ in Figure 1, the two open-drum IP local minimum structures that are unique to the zinc-rich compositions, closed upon structural relaxation (minimization of DFT energy) to the LM1 hexagonal prism. Interestingly, there is a change in the structural type for the DFT lowest energy $Zn_{6-m}Mg_mO_6$ clusters; before m = 2, the ring is more favorable than the drum. For both structural types, cation mixing is favored: in fact, all the different cation orderings are lower in energy, $E[Zn_{6-m}Mg_mO_6] < (6 - m)E[Zn_6O_6] + mE[Mg_6O_6]$. There is also little benefit (less than 0.08 eV/cluster) in a particular cation order: a slight tendency for the interatomic distances to be maximized between (a) the first two dopants in a drum and (b) two or three dopants in the ring. In contrast to zinc, magnesium cations are less stable in the low-coordinated sites of the 8-ring structure: the energy steadily increases with each substitution, 0.64 eV for the first Mg and 0.92 eV for the last Mg (energies relative to the drum structural type). Moreover, the three lowest energy points for the 2D edge-sharing hexagon−tetragon−hexagon cluster type, labeled "H-T-H" in Figure 2b, correspond to when Mg does not occupy any of the two-coordinated sites. The strong preference of Mg in the H-T-H structural type results in a large spread of solution energies, and for all cation configurations those energy points are above the broken line for H-T-H (energetically favorable for cation segregation); we find at least one Mg in a two-coordinated site that is furthest from the tetragonal ring.

Since the solution energy for the n = 4 cuboid increases dramatically as the content of magnesium decreases, a similar trend should be expected for the n = 6 cuboid or rock-salt fragment (labeled NaCl in Figure 2b). Although we expect the magnesium atoms will occupy the highest coordinated sites (i.e., bonded to four oxygen atoms), such configurations correspond to the highest, rather than lowest, set of energy points shown in Figure 2b for the cuboids. The energies of these points (which are connected by the upper line) steadily increase with content of zinc, from m = 6 to m = 2, as zinc oxide is less stable in the cuboid structural type. For m < 2, zinc atom(s) must also occupy the four-coordinated cation site, and so we expect the energy to increase more rapidly. These and the other cation configurations for the n = 6 cuboid, which are expected to have a higher energy, deform significantly about the zinc atom(s) that occupies the initially four-coordinated site(s). In fact, if these higher coordinated sites are occupied by zinc atoms, the four-coordinated cation sites become two-coordinated after relaxation; the four-coordinated oxygen atoms move outward (cuboid inflates) and only remain bonded to the three-coordinated cation sites. The effect is less dramatic if the other four-coordinated site is occupied by magnesium. Hence, the zinc atoms again tend to occupy the lower coordinated site (or environments where the coordinated oxygen atoms do not create O−Zn−O bond angles that are close to 90°), albeit by occupying the initially higher coordinated sites. The maximum interatomic distance between the four-coordinated oxygen anions and this cationic site is 2.18, 2.76, and 3.24 Å for m = 6, 4, and 0, respectively. Upon doping the inflated zinc oxide cuboid, composed of only two- and three-coordinated sites, magnesium atoms tend to occupy the three-coordinated sites. For m = 2, the magnesium atoms are in different tetragonal rings, opposite each other rather than furthest apart. Finally, one cationic configuration of the n = 6 cuboids—zinc cations along one face and magnesium cations along the opposite face for m = 3—is not stable and relaxes to form a drum.

dx.doi.org/10.1021/jp4084635 | J. Phys. Chem. C 2013, 117, 27127−27145

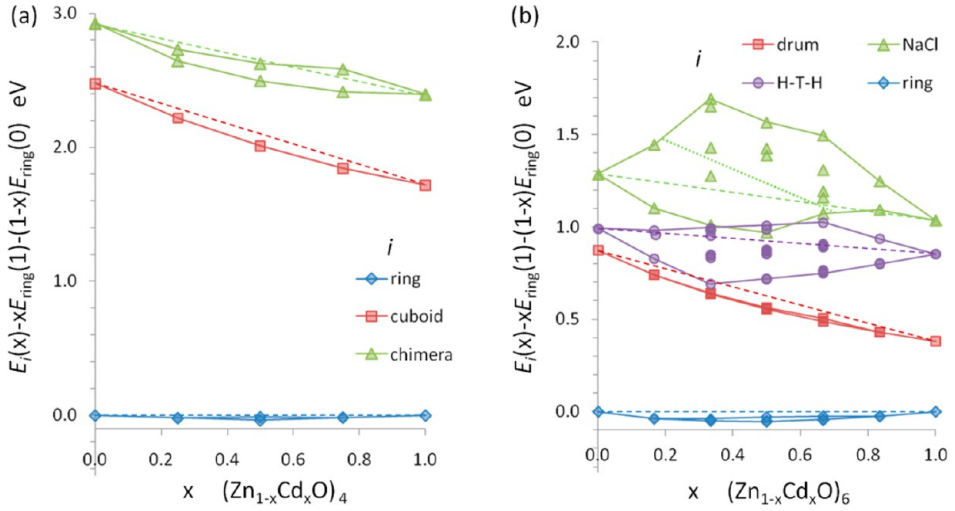

Figure 3. DFT solution energies, $\Delta E_i(x)$, for clusters of (a) $(Zn_{1-x}Cd_xO)_4$, and (b) $(Zn_{1-x}Cd_xO)_6$, where $E_i(x)$ is the total energy of configuration type *i*. The solid lines connect the highest and lowest values for each structural type; the broken lines represent the arithmetic mean energy of mixing end members (solution energy of zero for that structural type); and the seven triangles below the dotted line represent inflated cuboid structures.

The DFT energies obtained for the cadmium doped $n = 4$ zinc oxide clusters (see Figure 3a) suggest that there is only one important structural type, namely the ring. Although the difference in the solution energy for the rock-salt cut, or cuboid, decreases by 0.76 eV, the $(CdO)_4$ cuboid is still 1.72 eV higher in energy than the ring. A similar trend is found for the chimera structures (LM3); $(CdO)_4$ is 0.53 eV lower in energy than $(ZnO)_4$, and all LM3 clusters are approximately 0.5 eV higher in energy than the cuboids. Like Mg, Cd prefers the higher three-coordinated site in LM3—only the $ZnCd_3O_4$ LM3 structure with zinc occupying the three-cooridnated site has a positive solution energy with respect to its LM3 end members. The $(MgO)_4$ ring in Figure 1 resembles a regular octagon, whereas the DFT relaxed $n = 4$ rings are more square-like with oxygen atoms in the corners and cations in the center of the sides. The bond angles approach the ideal 90° and 180° for a square as magnesium is replaced with either cadmium or zinc (117.1°, 152.9° for Mg_4O_4; 100.9°, 169.1° for Cd_4O_4; 100.8°, 169.2° for Zn_4O_4). In contrast, the bond lengths for Zn_4O_4 (1.811 Å) are similar to those in Mg_4O_4 (1.831 Å), which are both smaller than those in Cd_4O_4 (2.037 Å). The (−Zn−O−Cd−O−Zn−O−Cd−O−) ring, where zinc and cadmium alternate about the ring, is 0.02 eV lower in energy (DFT) than the other $Zn_2Cd_2O_4$ ring, (−Zn−O−Zn−O−Cd−O−Cd−O−). For $n = 4$ clusters, only rings are expected to be observed at room temperature, with no preference for a particular cation order.

A different ranking was found for the lowest four LM $n = 6$ clusters of zinc and magnesium binary oxides: ring−drum−HTH−NaCl and drum−NaCl−HTH−ring, respectively. The lowest four LM for $n = 6$ cadmium oxide clusters have the same rank as zinc oxide. Hence, for the cadmium/zinc solutions there is no crossing in Figure 3b (rank change between structural types), just a slight overlap between favorable cation ordered NaCl clusters and unfavorable cation ordered H-T-H clusters for $m = 3$. As before, increasing the zinc content of the $1 \times 1 \times 2$ cuboid (composed of three tetragonal $n = 2$ rings) decreases its relative stability (energy points labeled NaCl in Figure 3b) unless the middle tetragonal ring inflates so that the coordination of the four-coordinated site(s) in the cuboid is reduced to two. Bonds are broken within the middle tetragon as one or both four-coordinated oxygen atoms move outward. Unlike the magnesium−zinc oxide $n = 6$ cuboids, this type of inflation does not occur if zinc occupies the cadmium preferred four-coordinated site(s). For the cadmium doped zinc oxide $n = 6$ cuboid clusters, inflation occurs if an initially four-coordinated oxygen atom is bonded to two three-coordinated zinc atoms (or bonded to just one three-coordinated zinc atom for one configuration of both Zn_5CdO_6 and $Zn_3Cd_3O_6$). The cation−anion interatomic distance within the inner tetragonal $n = 2$ ring; i.e., between the initially four-coordinated cadmium atoms and the oxygen atom(s) that moves outward, increases from 2.473 Å in Cd_6O_6 to 3.223 Å in $Zn_2Cd_4O_6$, 3.212 and 3.565 Å in $Zn_3Cd_3O_6$, 3.318 or 3.356 Å in $Zn_4Cd_2O_6$, 3.192 and 3.312 Å or 2.676 and 3.366 Å in Zn_5CdO_6, and 3.240 Å in Zn_6O_6. Without imposing symmetry constraints, two of the cuboids relaxed to the lower energy drum structure—$Zn_4Cd_2O_6$ with Cd in different sites and $Zn_3Cd_3O_6$ with Cd atoms on one face of the cuboid (and Zn on the opposite face). For each *m*, all of the inflated $n = 6$ cuboids are lower in energy (lowest triangles in Figure 3b for $m = 0$−4) than the clusters that maintain the original cuboid configuration composed of three- and four-coordinated sites. For the doped H-T-H structures, zinc atoms tend to bond simultaneously with both two- and three-coordinated oxygen atoms, whereas cadmium atoms occupy the higher coordinated sites and bond to three oxygen atoms.

For cadmium and zinc solutions, the hexagonal prism or drum configuration is always the second lowest energy structural type, although the energy gap between this structural type and the global minimum, the ring, decreases with increasing cadmium content. The energies calculated for the set of $Zn_4Cd_2O_6$ drums suggest that cadmium atoms prefer to be in the same tetragonal face, whereas for $Zn_2Cd_4O_6$ the zinc atoms tend to occupy the same hexagonal face. In the $Zn_3Cd_3O_6$ drum, it is cadmium's preference that prevails. After relaxation, the dodecagonal ring structures resemble hexagonal rings with oxygen atoms at the corners and cations in the center of each of the six sides. Like the $n = 4$ rings, the bond angles for Mg_6O_6, 134.6° and 165.6°, are further from those of the reduced regular polygon (in this case, 120° and 180°) than that found for the other end members: 116.2° and 183.8° for Zn_6O_6 and 115.3° and 184.7° for Cd_6O_6. Note that the O−Zn−O and O−Cd−O bond angles point inward. For the Zn−Cd mixed rings, the dopants prefer to

dx.doi.org/10.1021/jp4084635 | J. Phys. Chem. C 2013, 117, 27127−27145

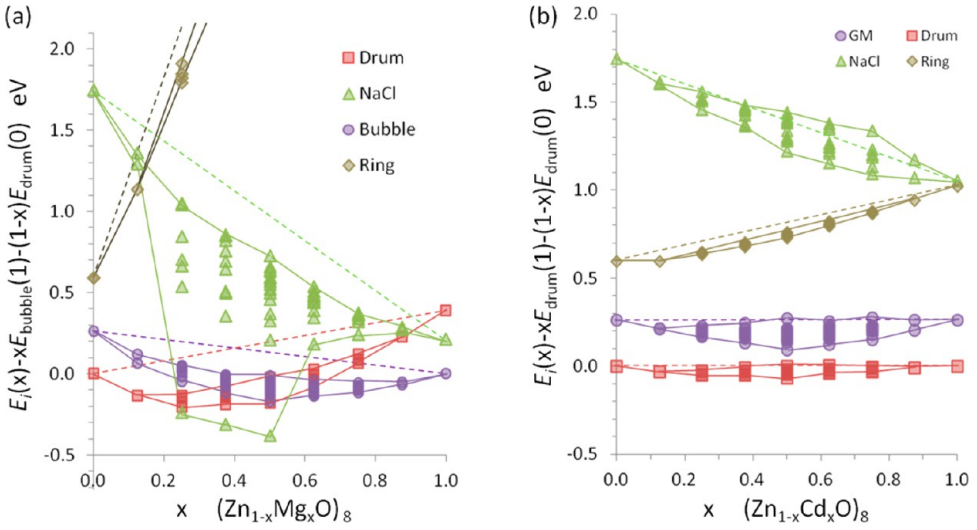

Figure 4. DFT solution energies, $\Delta E_i(x)$, for clusters of (a) $(Zn_{1-x}Mg_xO)_8$ and (b) $(Zn_{1-x}Cd_xO)_8$, where $E_i(x)$ is the total energy of configuration type *i*. The solid lines connect the highest and lowest values for each structural type; the broken lines represent the arithmetic mean energy of mixing end members (solution energy of zero for that structural type).

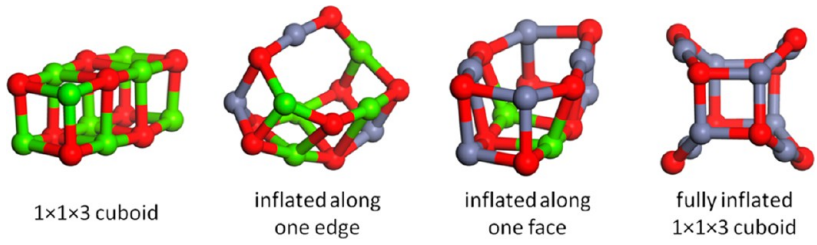

Figure 5. A set of $n = 8$ clusters, from a $1 \times 1 \times 3$ cuboid to the fully inflated $1 \times 1 \times 3$ cuboid.

maximize the distance between them, i.e., alternate for $m = 3$ and occupy opposite sides for $m = 2$ and 4, although the energy differences between different cation distributions is small (less than 1/100, 1/40, and 1/50 eV for $m = 2$, 3, and 4, respectively); likewise for the solution energy with respect to the end member rings (between 0.03 and 0.05 eV).

The solution energies for the $n = 8$ low-energy clusters are shown in Figure 4. The drum, or octagonal prism, is the lowest energy structure for most compositions: $Zn_{8-m}Mg_mO_8$ for $m = 0$ to 1 and $Zn_{8-m'}Cd_{m'}O_8$ for $m' = 0-8$. Although the rank predicted for the two lowest DFT energy Zn_8O_8 nanoclusters is the reverse to that defined by IP energies (see Figure 1), the change in rank is small and much higher ranked LM need not be refined with DFT. Interestingly, the rank predicted using NWChem (the package employed to calculate optical spectra; see next section) agrees with the IP model. A reversal of ranks is also seen for the Mg_8O_8 clusters, but this time the IP model ranks the drum as the GM whereas for DFT it is the bubble.

Upon doping the $(ZnO)_8$ drums with two magnesium atoms, the dopants tend to maximize the distance between them; i.e., the magnesium atoms occupy opposite sides of the *same* octagonal face for $m = 2$. The third magnesium atom tends to occupy the same tetragonal face with one the of previous magnesium atoms. This preferred cation ordering was predicted by the interatomic potential calculations (see Figure 1). Moreover, this agreement continues to $Zn_4Mg_4O_8$; the lowest energy structure has magnesium atoms in two tetragonal faces that are furthest from each other (likewise for the zinc atoms). The resulting drum has squashed octagonal faces, with a 4.951 Å diameter between magnesium atoms and 4.125 Å diameter between zinc atoms. Upon doping the $(MgO)_8$ drum with two zinc atoms, the dopants again prefer to maximize the distance between them, which is achieved by occupying *different* octagonal faces, although the same ordering is achieved for $m = 3$ and 5. A yet different preference is found for two cadmium atoms, which share tetragonal faces so to reduce the interatomic distance between dopants. Likewise for three cadmium dopants—all are on one side of the drum forming part of two edge sharing tetragonal faces.

The $n = 8$ bubble, LM1 and LM2 in Figure 1 for $(ZnO)_8$ and $(MgO)_8$, respectively, is composed of four hexagonal and six tetragonal faces, with all atoms coordinated to three others, and has two unique cationic sites: a cation can either be part of one hexagonal and two tetragonal faces, site A, or one tetragonal and two hexagonal faces, site B. As a dopant both magnesium and zinc prefer to occupy site A and to maximize the distance between themselves (the second dopant occupies the furthest A site from the first dopant for $m = 2$ and 6). When there are three or more zinc atoms, more stable configurations are obtained if the zinc atoms occupy the B sites. For bubble clusters containing cadmium atoms, the B sites, where possible, are occupied by cadmium atoms and, as found for the drum structures, Cd dopants prefer to minimize their interatomic distance.

The $1 \times 1 \times 3$ cuboid has two unique sites: the three-coordinated corner sites and the four-coordinated edge sites. Not surprisingly, $n = 8$ cuboids for both magnesium and cadmium oxides are energetically more favorable, by 1.27 and 0.69 eV, respectively, than that for zinc oxide. As dopants the first four cadmium atoms prefer the higher coordinated sites, with the second dopant on the same face as the first. Because of the strain

dx.doi.org/10.1021/jp4084635 | J. Phys. Chem. C 2013, 117, 27127−27145

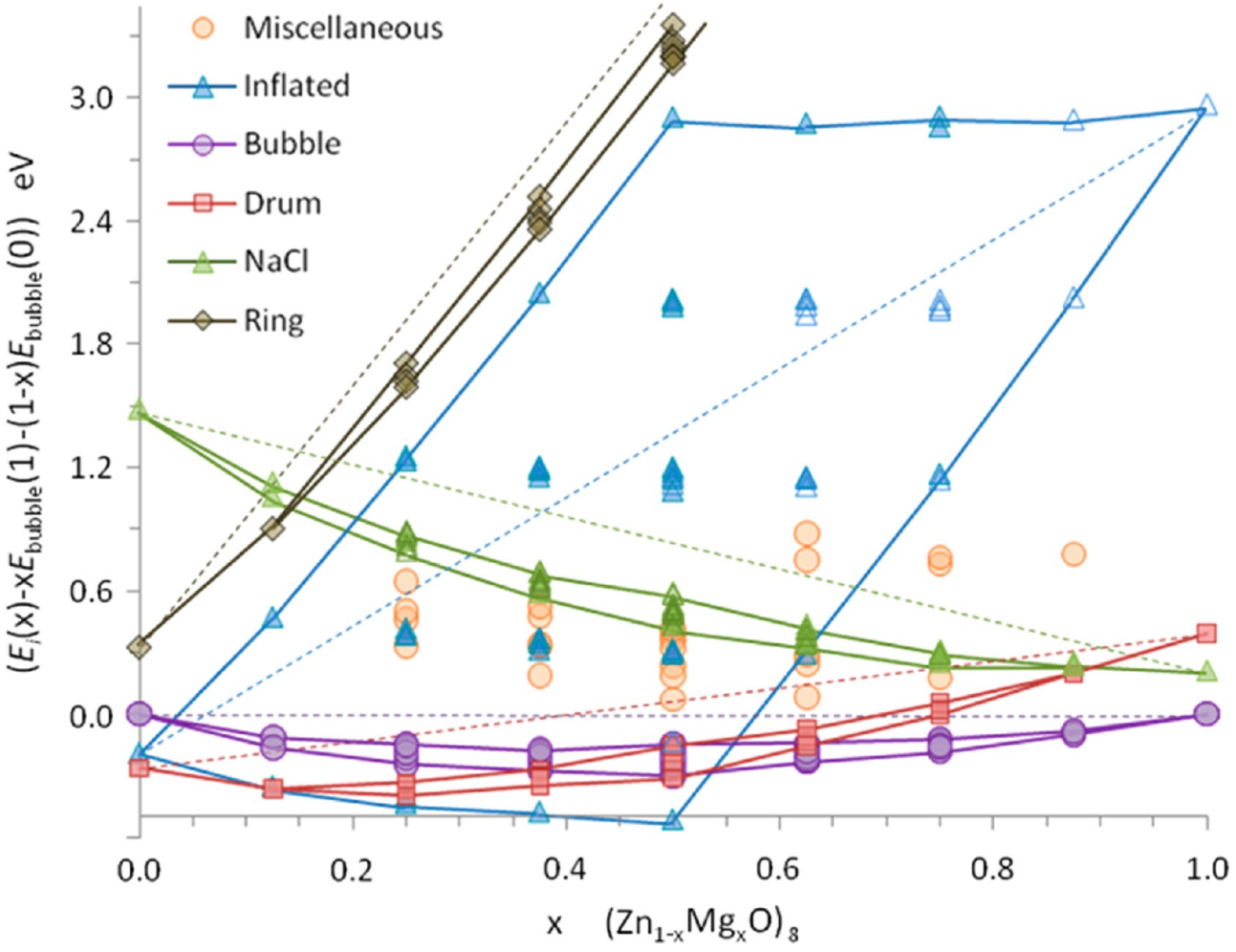

Figure 6. DFT solution energies, $\Delta E_i(x)$, for $(Zn_{1-x}Mg_xO)_8$ clusters, where $E_i(x)$ is the total energy of configuration type i (including the additional/redefined structural types—cf. Figures 4 and 5). The solid lines connect the highest and lowest values for each structural type; the broken lines represent the arithmetic mean energy of mixing end members (solution energy of zero for that structural type); and unfilled symbols, together with a darker lined triangle in in the special case of NaCl structural type, represent clusters that will readily relax to a different structural type, which include partially inflated rock-salt cuts that are labeled as miscellaneous.

caused by the difference in cation sizes, the inverse cationic order for $(Zn_4Cd_4O_8)$ with all zinc atoms occupying the edges is actually a better arrangement than alternating planes of cations. As with cadmium, the first magnesium atom prefers an edge site and the last zinc atom the corner site. In both systems with just one zinc atom, the zinc atom prefers the corner site. The energy points obtained by relaxing the cuboid zinc−magnesium system form two separate groups—the NaCl (cuboid) data set in Figure 4a. The smaller group of data points are much lower in energy and indicative of a significant structural change. Moreover, the energies of the smaller subset are even lower than those calculated for the drum and bubble structural types. Examination of the final structures for this subset of low-energy points revealed that the cuboid had in fact inflated and identified as a different structural type—in Figure 1 it is shown as LM5 for $(ZnO)_8$. Running the genetic algorithm to search for the magnesium−zinc oxide structures also readily finds these and other partially inflated structures (see Figure 5). For the $(ZnO)_8$ cluster, the Zn−O interatomic distances are 2.0 Å within the end plane (tetragonal ring of four atoms) and 2.3 and 2.8 Å within a middle plane of a relaxed and an inflated cuboid, respectively.

Reclassifying the NaCl data in Figure 4a and including additional data (obtained by imposing the pseudosymmetry of the cuboid or inflated cuboid during relaxations from these two structural types), a clearer picture is obtained (see Figure 6). The data set labeled NaCl is now more compact, and there is a pleasing symmetry to the spread of energy points for the fully inflated clusters. We note that many of these points are not filled indicating that they will relax to a different structural type if not constrained. For example, the magnesium-rich inflated clusters collapse to the cuboid. The preference in the inflated clusters is the reverse to that found in the cuboid with zinc atoms preferring the two-coordinated edge sites and magnesium atoms the corner sites. In the partially inflated structures, typically the zinc atoms occupy the edge site on the inflated side and magnesium atom on the collapsed side. Note that we only report metastable clusters for the partially inflated structures—labeled as miscellaneous in Figure 6.

The stability of rings decreases with size and content of both cadmium and especially magnesium. Mg containing ring structures undergo a transition from a planar to a corrugated motif: as the concentration of Mg content is reduced, the 2D ring becomes a crown (alternating, anions displace above and then below the ring of cations). If this structural type were adopted by the Zn:Mg system, the shortest interatomic distances between cations of the same species would be maximized. In Zn:Cd,

dx.doi.org/10.1021/jp4084635 | J. Phys. Chem. C 2013, 117, 27127−27145

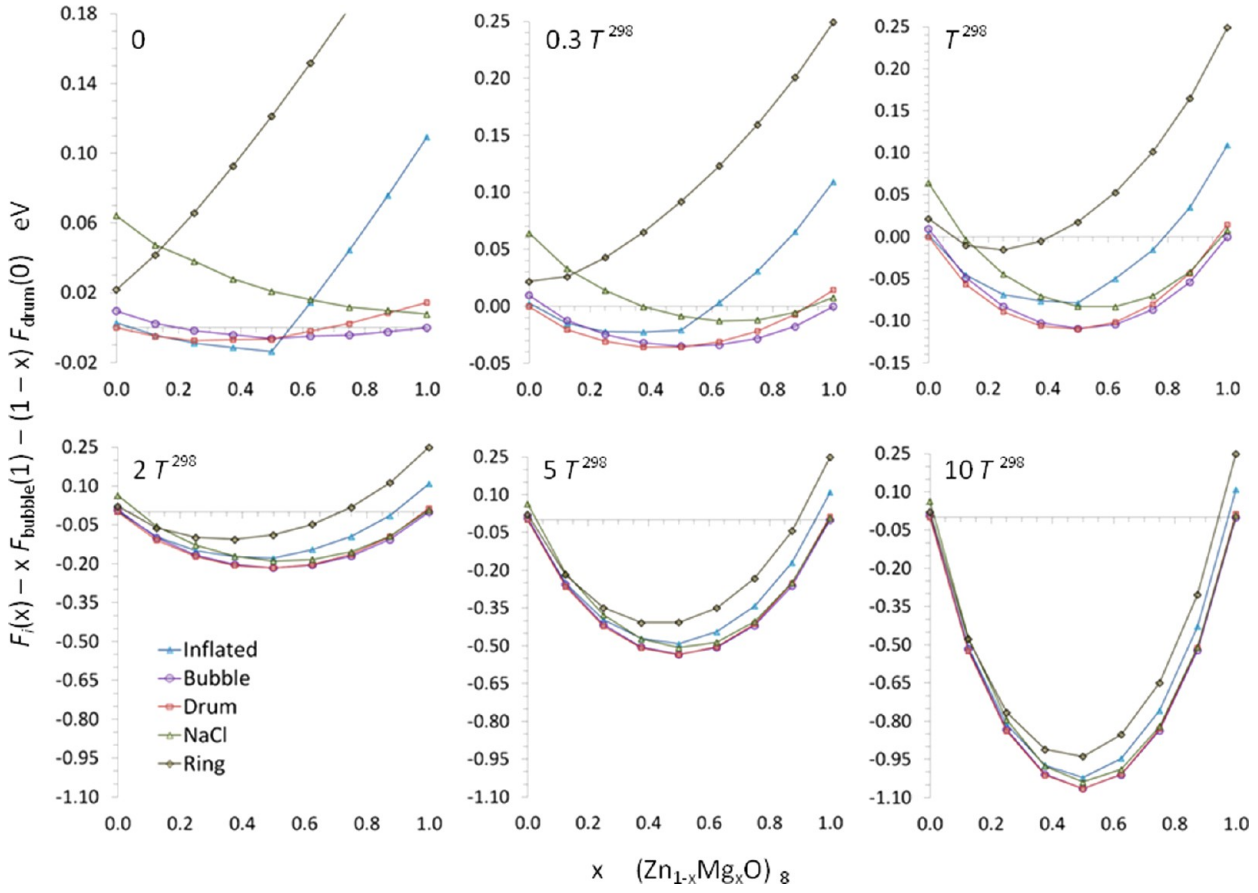

Figure 7. Free energies of solution, ΔF, for $(Zn_{1-x}Mg_xO)_8$ cluster types calculated on a DFT potential energy landscape over six temperatures indicated in the graphs relative to room temperature, T^{298}, where $F_i(x)$ is the total free energy of structural type i.

solution energies are very similar for cation arrangements of the same composition. However, there is still a small penalty for configurations with like cations occupying nearest sites.

Finally, we investigate the configurational entropic effects, separately for each structural type, with the free energy defined as

$$F_i(x) = E_i^{GM}(x) - k_B T \ln Z_i(x) \quad (2)$$

where GM indicates the global minimum for a particular structural type i and composition x, k_B is the Boltzmann constant, T is temperature and Z is the partition function:

$$Z_i(x) = \sum_j m_i^j(x) \exp\{-(E_i^j(x) - E_i^{GM}(x))/k_B T\} \quad (3)$$

Note that the summation is over all unique configurations for a particular composition and structural type, m is the degeneracy of each unique configuration, and E is the total energy of the individual nanocluster. Moreover, we note that thermal motion contributions to the free energy are not included. To compare the relative stabilities of the structural types across the range of Zn:Mg compositions, we compute the solution energy similar to that in eq 1 but referenced to free energies and the energy scale based on the GM for $(ZnO)_8$ and $(MgO)_8$:

$$\Delta F_i(x) = F_i(x) - xF_{bubble}(1) - \{1 - x\}F_{drum}(0) \quad (4)$$

ΔF is plotted for $(Zn_{1-x}Mg_xO)_8$ nanoclusters and six different temperatures in Figure 7.

At zero temperate, the lowest free energy structural type changes from drum to the fully *inflated* 1 × 1 × 3 cuboid at x = 0.25 and then to a bubble for the magnesium-rich compositions. These curves have the same profile as seen in Figure 6 for the lowest energy members of each set; in particular, there is a sharp change in the free energy slope for the inflated cuboid at x = 0.5, a minimum at x = 0 (zinc-rich) for rings, and a minimum at x = 1 (magnesium-rich) for the 1 × 1 × 3 cuboid. As temperature increases, there is a downward shift in the free energy for the ternary compositions, and a minimum for each structural type moves toward x = 0.5. As there is a much greater species dependent ordering in the inflated cuboid structural type, the configurational entropic contribution to the free energy is smaller than that found for the bubble and the drum. At ~90 K, the drum is the GM structural type for zinc-rich compositions, and both drum and bubbles are dominant at x = 0.5 (inflated cuboid no longer has lowest free energy). As temperature increases further to room temperature, T^{298}, and above, the drum and bubble curves remain most stable for all compositions and appear to overlap. The drop in the free energy for all structural types becomes the dominant feature as the energy separation between structural types stabilizes above 2 T^{298}, which could be attributed to the configurational entropic contribution to the free energy becoming dominant.

4. EFFECT OF DOPING ON OPTICAL ABSORPTION

Doping zinc oxide with Mg or Cd is of primary applied interest due to the effect of impurities on optical properties. As mentioned earlier, bulk Mg doping results in a blue shift of absorption spectra while Cd doping yields the red shift. We focus on how the cluster morphology and size affect the optical absorption.

dx.doi.org/10.1021/jp4084635 | J. Phys. Chem. C 2013, 117, 27127−27145

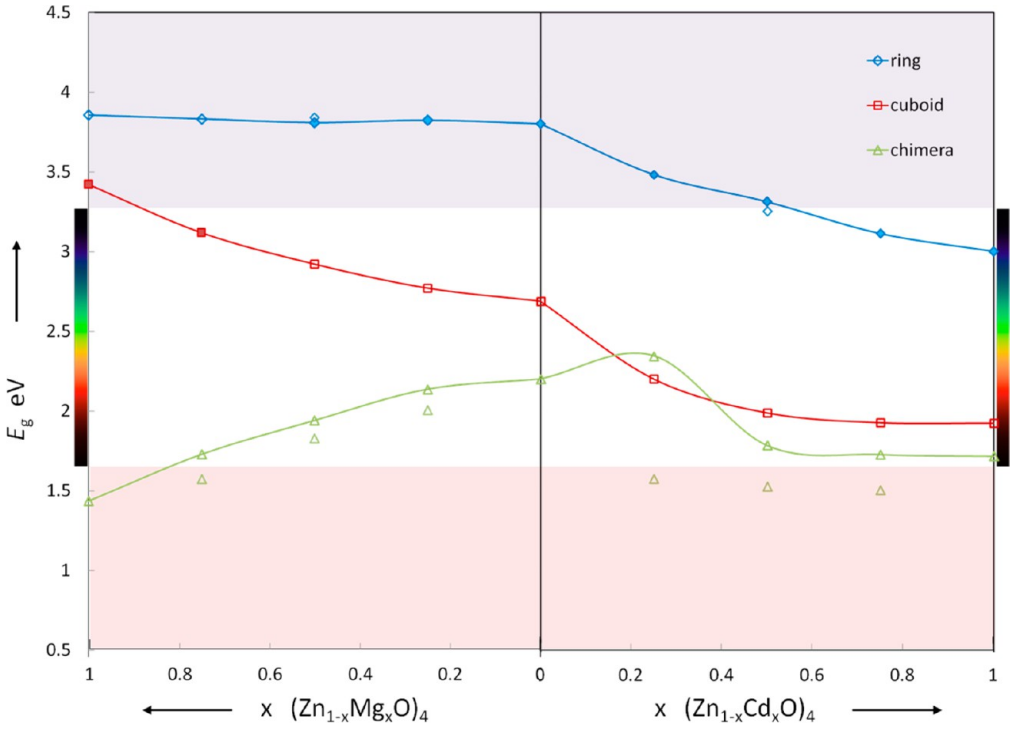

Figure 8. Lowest excitation energies for $(Zn_{1-x}Mg_xO)_4$ and $(Zn_{1-x}Cd_xO)_4$ clusters as a function of cluster stoichiometry (x) and morphology. For lowest PBE0 energy configurations in each structure family and stoichiometry, results are shown using filled marks connected by smooth lines. Higher energy configurations are denoted with open marks. The white band in the diagram highlights energies within the visible optical range.

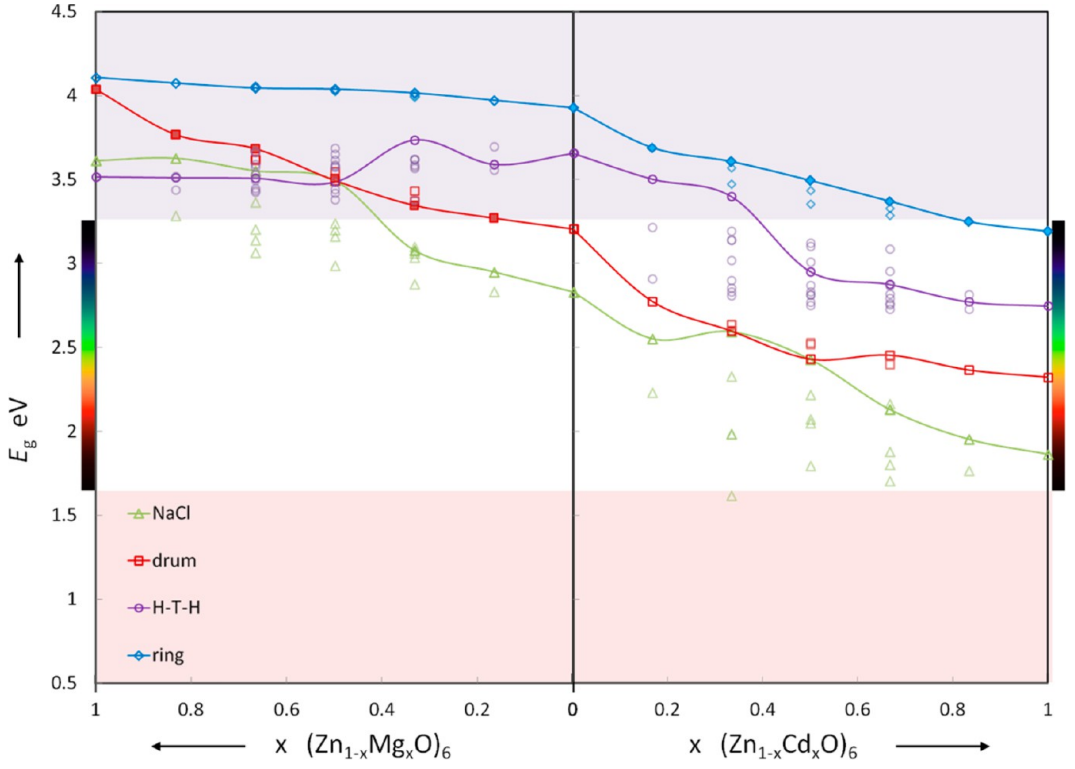

Figure 9. Lowest excitation energies for $(Zn_{1-x}Mg_xO)_6$ and $(Zn_{1-x}Cd_xO)_6$ clusters as a function of cluster stoichiometry (x) and morphology. Open marks are 50% transparent: a higher density of marks appears darker. See caption to Figure 8 for further conventions.

In general, the fundamental edge of absorption of bulk materials is controlled by the one-electron, delocalized, conduction and valence states. On the other hand, it can be influenced by the localized defect states with optical transitions between a defect and one of the bands, typically having a one-electron nature (the interaction between a hole and an excited electron is negligible). Therefore, electron ionization and affinity control the energies (wavelengths) of the absorbed light. In small

dx.doi.org/10.1021/jp4084635 | J. Phys. Chem. C 2013, 117, 27127−27145

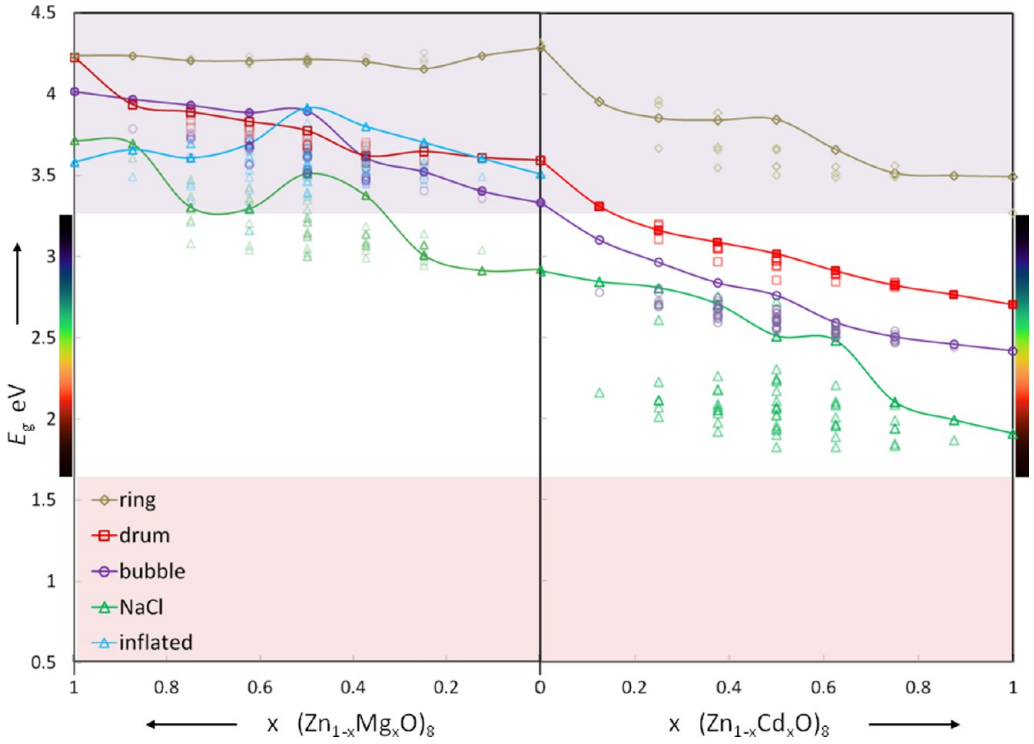

Figure 10. Lowest excitation energies for $(Zn_{1-x}Mg_xO)_8$ and $(Zn_{1-x}Cd_xO)_8$ clusters as a function of cluster stoichiometry (x) and morphology. Open marks are 50% transparent: a higher density of marks appears darker. See caption to Figure 8 for further conventions.

clusters, the electron−hole interactions are not weak, and an appropriate treatment is required to model relevant excited states. For this purpose we have used time-dependent DFT (TD DFT) as implemented in the NWCHEM code.[82]

The lowest energy excitations in II−VI compounds are typically of a charge-transfer nature. Such transitions are poorly described with standard LDA or GGA functionals, which (i) introduce unbalanced self-interaction errors in occupied valence states localized on anions and unoccupied (virtual, excited) states on cations and (ii) present a qualitatively wrong description of the asymptotic tail of the exchange-correlation potential, which affects directly the calculated excitation energies. These problems are effectively remedied using hybrid exchange and correlation functionals, which admix a nonlocal Hartree−Fock-like exchange (HF) to the energy functional and the corresponding kernel within the TD DFT approach. As our total energies, used to evaluate the quality of structures in the first part of this study, have been obtained using a nonempirical "general purpose" PBE functionals,[79] we choose to employ a matching PBE0 hybrid functional (factoring in 25% of HF exchange).[83] Furthermore, to improve the description of the delocalized states, we employed a Cassida−Salahub asymptotic correction[84] with the numerical value of the shift calculated by the code automatically using a semiempirical formula of Zhan, Dixon, and Nichols.[85] This latter correction in all our calculations proved to be minor, less than 1% of the total excitation energies.

The NWChem code employs Gaussian basis functions and effective core potentials. We have chosen a Def2-TZVP basis on O and Mg and a TZVP quality basis set[86] associated with a relativistic small-core pseudopotential from ref 87 on Zn and Cd.

The optical calculations have been performed for the geometries optimized at the PBE level of theory, with three lowest singlet states of interest included under consideration and no symmetry constraints. Our results are shown as Figures 8−10.

To understand the causes of the variations, or trends, we have also investigated the charge density distribution of the lowest-energy exciton (an electron and hole pair) for a number of key clusters. We note that this exciton can be degenerate or quasi-degenerate (typically, with energy levels separated by less than 0.1 eV) (see Figure 11) in which case we take the state average. For the purpose of visualization, we employ charge density differences of the ground and excited states of interest.

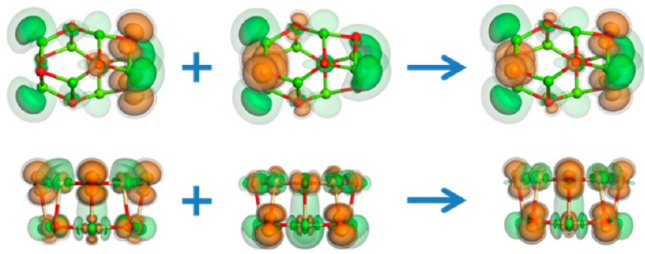

Figure 11. Two examples, Mg_8O_8 bubble and Cd_8O_8 drum, where the lowest energy excitons are degenerate. In these examples and below we generate state average representations of such states. Excited electron (green) or hole (orange) components are shown as isosurfaces of charge density differences with values of 0.01 (slightly transparent), 0.001 (more transparent), and 0.0005 e/bohr^3 (most transparent). Note Mg, Zn, Cd, and O ions are represented by small spheres colored green, gray-blue, cream, and red, respectively.

Let us consider the structural variation in the ring configurations for Mg, Zn, and Cd. Employing a rigid ion model, with no electronic polarization, the rings resemble regular n-sided polygons; for example, n = 4 resembles an octagon. In contrast, the rings obtained with the shell model are distorted to an $n/2$-sided polygon;[65] the octagon transforms into a square-like structure with the anions displacing further away from the

dx.doi.org/10.1021/jp4084635 | J. Phys. Chem. C 2013, 117, 27127−27145

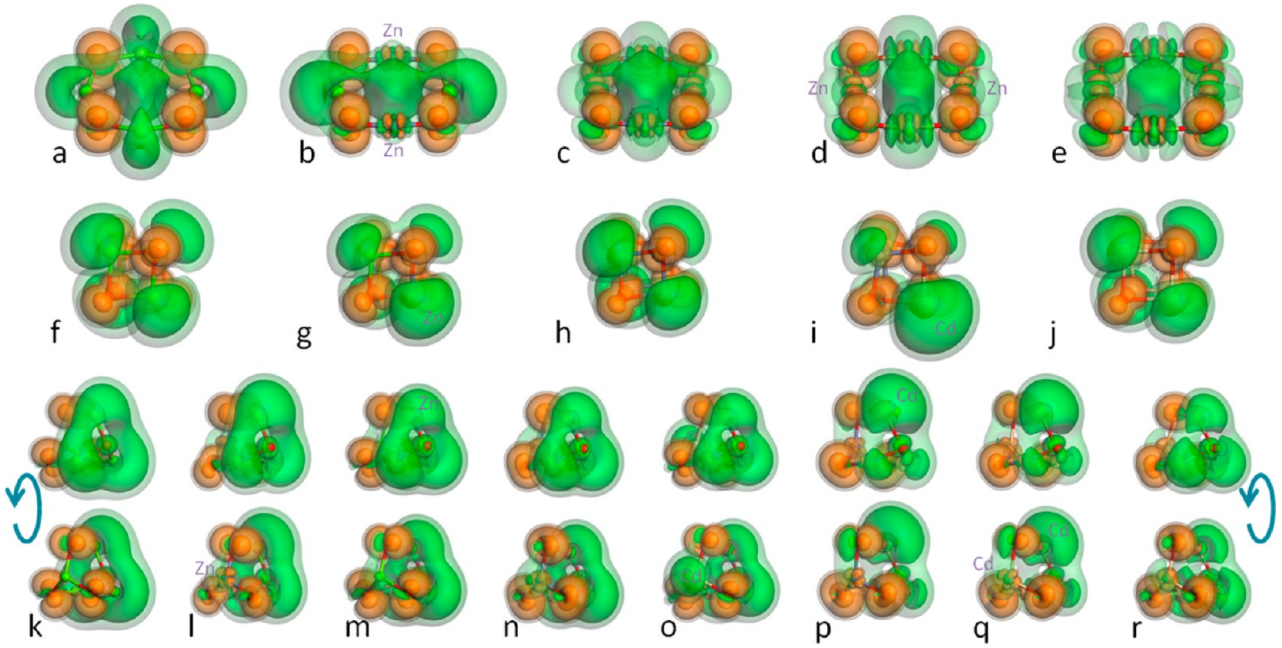

Figure 12. Charge density difference of the lowest energy exciton for (a) Mg_4O_4, (b) α-$Mg_2Zn_2O_4$, (c) Zn_4O_4, (d) α-$Zn_2Cd_2O_4$, (e) Cd_4O_4 rings; (f) Mg_4O_4, (g) Mg_3ZnO_4, (h) Zn_4O_4, (i) Zn_3CdO_4, (j) Cd_4O_4 cuboids; and (k) Mg_4O_4, (l) α-Mg_3ZnO_4, (m) β-Mg_3ZnO_4, (n) Zn_4O_4, (o) α-Zn_3CdO_4, (p) β-Zn_3CdO_4, (q) $Zn_2Cd_2O_4$, (r) Cd_4O_4 chimeras, where α and β indicate the lowest and second lowest energy cation ordering, respectively. See caption to Figure 11 for further conventions.

center of the ring (bond angles nearer 90° and 180° than 135°). The shells on the anions displace inward so as to reduce the distance to the nearest cation sites. This transformation is enhanced if we also allow the cations to polarize—we set the polarizability of the cation to be much less than that of the anion—as the shells on the cations will move outward while the cations themselves move inward. Considering the three pure $(XO)_4$ rings, the Mg ions are least polarizable and Cd ions most; at the same time the oxygen ions coordinated to Mg are least polarizable and those to Cd most due to relative electronegativities of the cations—an effect that results in the more acute bond angle centered on O. Therefore, we should expect, and do observe, the MgO structure most resembling an octagon (Mg−O−Mg = 117°, O−Mg−O = 153°). The CdO and ZnO structures, which resemble more a square, both have bond angles X−O−X of 101° and O−X−O of 169°, but of course very different bond lengths (which in turn increases the X−O−X bond angle for a given O polarizability). As with the anion shell positions, the excited electron occupies the center of the ring; for the Cd and Zn systems the electronic state resembles a cylinder that is dented/distorted by the presence of the atoms (see Figures 12a−e). (This electronic state is reminiscent of the electron localizing on the anionic vacant sites in alkali halides or alkali earth oxides, forming F centers.) As the Cd content increases, so does the ring size, and the overlap of the excited electron and the corresponding cylinder decreases; likewise the energy of this excitation decreases (see Figure 8). As the Mg content increases, the excitation energy and the diagonal O−O distance remain fairly constant (5.10−5.03 Å) with the additional croissant-like lobes appearing on the outside of the ring on Mg ions. As we will see in other clusters, the excited electron tends to localize on outer cations that form the sharpest O−X−O bond angle.

Next we consider the effect of doping either the MgO cuboid (lowest energy configuration) with Zn or ZnO cuboid with Cd. The decrease in the excitation energy is smaller for each additional dopant in the cuboid as the excited electron prefers to sit on the outside of *all* Zn cations in the mixed Zn:Mg compounds and outside *all* Cd cations in the Zn:Cd compounds. Ignoring cation ordering, for both the ring and cuboid structural types there is only one unique site, all oxygen anions donate charge (see orange-colored surfaces in Figure 12).

For the chimera structural type there are two different sites for anions and likewise for cations. We find the lowest energy excitations involve electron transfer between the lower coordinated atoms. The excited electron localizes outside the cluster, mainly on *all* two-coordinated Cd cations, with the electronic lobes merging to form a triangular bagel for the smaller sized clusters that do not have any Cd content. The Zn_3CdO_4 chimera, with Cd on the higher-coordinated site, is the only exception to this trend. Another surprise is that part of the excited electron density appears just off the two-coordinated oxygen anion; this is particularly noticeable if this oxygen anion is bonded to a two-coordinated Cd cation. The most interesting observation is that the lowest excitation energy increases stepwise by ∼0.1 eV with decreasing Mg content or when Mg is switched from the higher- to a lower-coordinated site. The latter is expected, as the higher-coordinated site does not play a significant role in the excitation, so doping it with zinc has little effect on the excitation energy, whereas the influence on the excitation is pronounced if zinc is doped into one of the three two-coordinated sites. An increase in the excitation energy with the Zn content is opposite to that expected from bulk results. A closer inspection of the Zn:Mg chimeras reveals that the hole on the two-coordinated oxygen anions is dumbbell-like (one *p* orbital per atom) if the oxygen is directly bonded to a two-coordinated Mg cation and ring-like (mixture of two *p*-orbital densities) if directly connected to Zn (or Cd). There is also an increased presence, albeit small, of the excited electron over the back of the cluster (opposite side to the triangular bagel).

dx.doi.org/10.1021/jp4084635 | J. Phys. Chem. C 2013, 117, 27127−27145

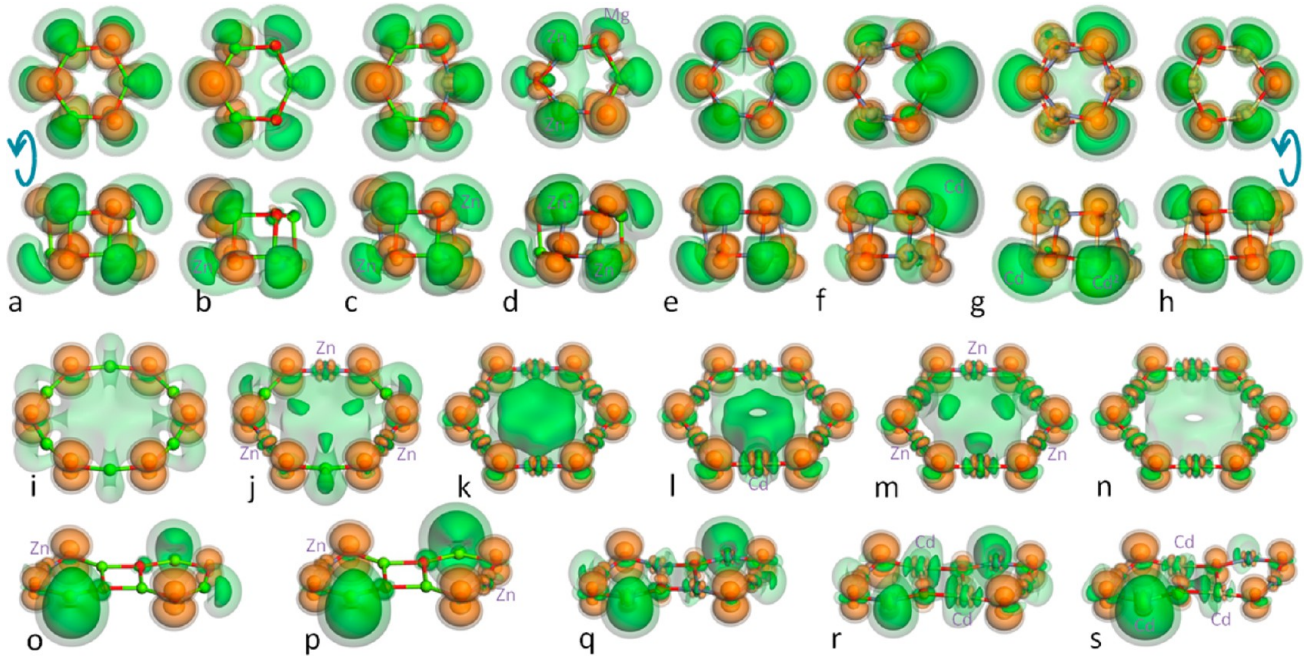

Figure 13. Charge density difference of the lowest energy exciton for (a) Mg_6O_6, (b) Mg_5ZnO_6, (c) α-$Mg_4Zn_2O_6$, (d) α-$Mg_3Zn_3O_6$, (e) Zn_6O_6, (f) Zn_5CdO_6, (g) α-$Zn_3Cd_3O_6$, (h) Cd_6O_6 drums; (i) Mg_6O_6, (j) α-$Mg_3Zn_3O_6$, (k) Zn_6O_6, (l) Zn_5CdO_6, (m) α-$Zn_3Cd_3O_6$, (n) Cd_6O_6 rings; and (o) α-Mg_5ZnO_6, (p) α-$Mg_4Zn_2O_6$, (q) Zn_6O_6, (r) α-$Zn_4Cd_2O_6$, (s) α-$Zn_3Cd_3O_6$ H-T-H clusters. See caption to Figure 11 for conventions.

Importantly, comparing the triangular bagels in front of the Mg and Zn two-coordinated cations, we observe that the excited electron is slightly more dispersed in front of Mg cations. This is also opposite to that observed for the cuboids—see Figure 12g, which shows an excited electron in the Mg_3ZnO_4 cuboid—indicating that the increased excitation energy is related to the decreased spread of the excited electron, which leads to the increase in its kinetic energy. For the Cd:Zn systems, there is also an increase in spread of the excited electron and a decrease in excitation energy as the two-coordinated sites are doped with Cd cations. As seen in the previous structural types, the largest effect on the excitation energy occurs when the first of any similar sites is filled by Cd (x = 0−0.8 for the higher energy configurations, unconnected data points, and x = 0.2−1.0 for the lower energy configurations, connected data points in Figure 8). Upon doping the chimera with Cd on the high-coordinated site, the excitation energy increases as a significant part of the excited electron is delocalized now onto the back of the cluster (assuming the triangular bagel remains at the front).

For the ring, drum, and rock-salt n = 6 structural types, a general trend is predicted for reducing the lowest excitation energy in the sequence from Mg to Zn to Cd oxides, which is however not followed by the H-T-H structural type (see Figure 9). Both ring exciton components, the hole in the form of dumbbells aligned perpendicular to the ring plane on all anions, and the electron confined mainly within the ring, are similar to those already described for the n = 4 rings. Moreover, in a pure ZnO cluster, the electron is again delocalized within the ring in an F-center like configuration (see Figure 13k). On doping with either Mg or Cd, although the delocalized character of the excited electron density is retained, there is a shift of concentration from Zn to the dopants, forming both in-ring and out-of-ring lobes around Mg ions, and in contrast only in-ring lobes near Cd cations (see Figure 13j,m). The key difference is the size of the rings; with increasing Cd content in the n = 6 rings, the excited electron does not occupy the very center—the cylinder becomes a tube (a cavity appears in the "F center")!

As with the rings, there is a clear similarity between n = 6 drums and n = 4 cuboids; the latter could also be considered as a double four-ring. The lobes of the hole and excited electron themselves and the changes to these lobes due to doping follow the same pattern outlined above: the lobes of the excited electron, although observed on all cations, are larger on Zn cations than on Mg and largest on Cd; and the excited electron is not found inside any of the drum or cuboid cages. One new feature found with the drums is the overlapping of lobes across tetragonal and hexagonal faces, for example: (i) between Cd cations across a hexagonal face if only partially doped (cf. Figure 13g,h); (ii) likewise between Zn cations for the Mg:Zn drums (Figure 13d); (iii) in fact, the lobes of Zn and Mg across an hexagonal face overlap in a Mg_5ZnO_6 drum (see Figure 13b); and (iv) across a Mg_2O_2 tetragonal face if a neighboring tetragonal face contains a Zn cation.

Like the chimera, the H-T-H structure has more than one unique ion site: two three-coordinated sites per cation, two two-coordinated (A) sites that connect to two two-coordinated oxygen anions, and two two-coordinated (B) sites that connect to one two-coordinated oxygen anion and one three-coordinated anion; likewise for anions. We note that the internal bond angles of B sites are smaller (more acute) than those of the A sites and, thus, more likely to host the hole and excited electron than the A sites. The holes in these structures are composed of dumbbell-shaped lobes on the anionic sites, the largest on the B sites, and the smallest on three-coordinated sites (the latter dumbbells vanish if Mg cations occupy both three-coordinated cationic sites). The largest lobe(s) for the excited electron is always largest on the B cationic sites for all cluster compositions and orderings, accompanied by a small lobe on the three-coordinated anions. If a Cd or Zn ion occupies one of the three-coordinated sites, the electron also has lobes around these sites, which spread across the tetragonal ring if both sites are Mg-free.

dx.doi.org/10.1021/jp4084635 | J. Phys. Chem. C 2013, 117, 27127−27145

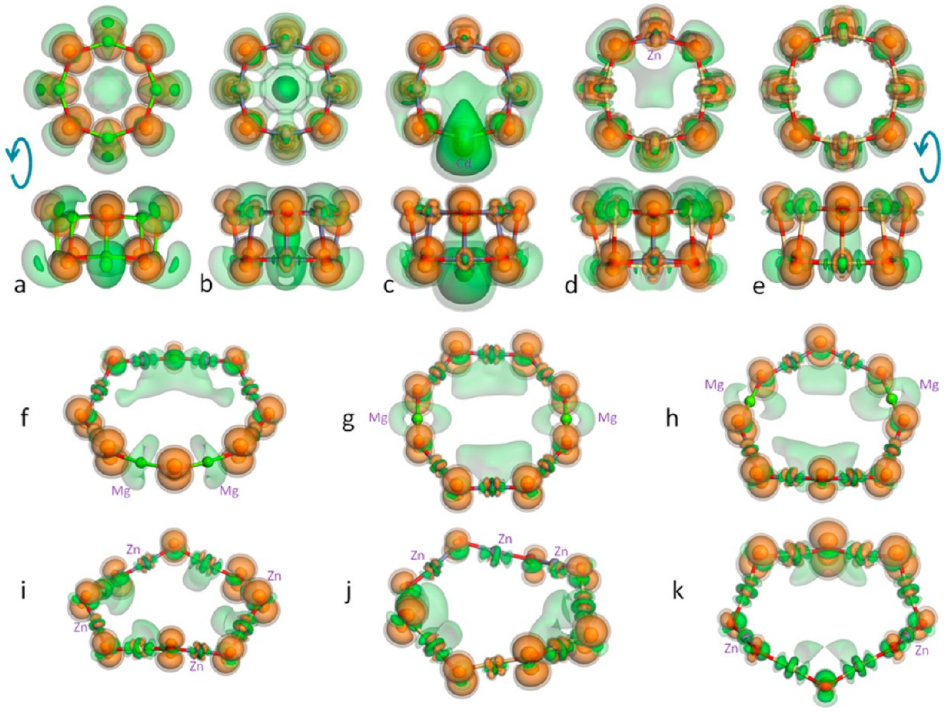

Figure 14. Charge density difference of the lowest energy exciton for (a) Mg_8O_8, (b) Zn_8O_8, (c) Zn_7CdO_8, (d) $ZnCd_7O_8$, (e) Cd_8O_8 drums; and (f) δ-$Mg_2Zn_6O_8$, (g) α-$Mg_2Zn_6O_8$, (h) β-$Mg_2Zn_6O_8$, (i) α-$Zn_4Cd_4O_8$, (j) α-$Zn_3Cd_5O_8$, (k) α-$Zn_2Cd_6O_8$ rings. In the lower projection of (c) and (d), the dopant is at the back and front, respectively. See caption to Figure 11 for conventions.

In the rings, the lowest excitation energy (E_g) decreases with Cd content, although the rate of change is reduced by the ordering that maximizes the distance between Cd ions—for Zn:Cd ratio (value of x) the lowest data point corresponds to the cation segregation (Cd on one side of the ring). A similar decrease in E_g with Cd content is seen in the drums, but now the rate of change is influenced by whether the Cd ions are all in one or both hexagonal rings. Considering only the lowest energy drum configurations, E_g of $Zn_2Cd_4O_6$ is actually greater than that of $Zn_3Cd_3O_6$ as the additional Cd ion occupies at least one of the sites in the second hexagonal face. The kink in the drum's curve at $Zn_2Mg_4O_6$, although not as dramatic, is also caused by the preferred cation ordering. The lowest energy cation ordering maximizes the distance between the two Zn cations in the $Zn_2Mg_4O_6$ drum; higher-energy cation arrangements have a lower value of E_g. For the $Zn_4Mg_2O_6$ drums, the lowest-energy cation ordering maximizes the distance between the two Mg cations and higher-energy cation arrangements have a higher value of E_g. Finally, we consider the purple line in Figure 9, i.e., the changes in E_g across the series of lowest-energy cation-ordered H-T-H structures. Starting from Mg_6O_6, there is a significant increase in E_g from $Zn_3Mg_3O_6$ to $Zn_4Mg_2O_6$ and a significant decrease from $Zn_4Cd_2O_6$ to $Zn_3Cd_3O_6$. The former relates to a Mg cation no longer occupying the B cationic site (where the excited electron has the largest lobe), and the latter can be attributed to Cd cation occupying this site. From our results for the different cation-ordered, singly doped H-T-H structures, we can see that the dependence of E_g on cation order is more complex than the occupancy of this B cationic site; the largest decrease (increase) in E_g occurs when the Zn dopant is moved into the tetragonal ring (Mg dopant is moved to the A cationic site).

For the $n = 8$ structural types, we again find the general trend of the first excitation energy decreasing in the sequence from Mg to Zn to Cd oxides. Focusing on the lines drawn in Figure 9 (showing E_g data for the most stable cation-ordered members of each structural type and composition), there are noticeable exceptions to this trend as E_g has a maximum cusp at Zn_8O_8 in the ring and drum series; a maximum at $Zn_4Mg_4O_8$ for the inflated structural type; a step between $Zn_4Mg_4O_8$ and $Zn_5Mg_3O_8$ in the bubbles; and a cusp at $Zn_4Cd_4O_8$ in the rings. The largest spread in the DFT solution energies was found for the rock-salt (labeled NaCl) structural type, so not surprisingly the E_g for the NaCl structural type has the largest scatter (see Figures 4 and 9). A closer inspection of E_g for a series of Zn:Mg inflated rock-salt structures revealed two competing factors: E_g increases with Mg concentration and with the number of Zn cations that occupy the two-coordinated sites. Note that E_g increases upon doping Mg_8O_8 with one Zn cation on a two-coordinated site but decreases if Zn occupies a four-coordinated site; the lowest energy $Zn_2Mg_6O_8$ inflated configuration has one Zn cation on the two-coordinated site (hence only the second highest value of E_g for this stoichiometry), and all two-coordinated sites are occupied by Zn cations in the lowest energy $Zn_4Mg_4O_8$ (for which E_g has a maximum) and zinc-rich clusters.

Exciton components on the $n = 8$ rings (or crowns) are similar to those already seen on the smaller rings (cf. Figures 12a–e, 13i–n, and 14f–k). The hole has the shape of dumbbells aligned normal to the ring plane on all anions. The electron localizes predominantly within the ring, although no longer reaching its center, and forming: (i) merged lone-pair type lobes that delocalize between neighboring Zn cations in Zn:Mg; (ii) lone-pair type lobes on Cd in Zn:Cd; and (iii) bagel-like nodes around all Mg cations. Furthermore, the Zn and Cd cations host some of the excited electron density in antibonding sigma orbitals, and the size of the dumbbell basins is dependent on the neighboring cation. In the Zn:Mg series, we observe a nearly constant

dx.doi.org/10.1021/jp4084635 | J. Phys. Chem. C 2013, 117, 27127–27145

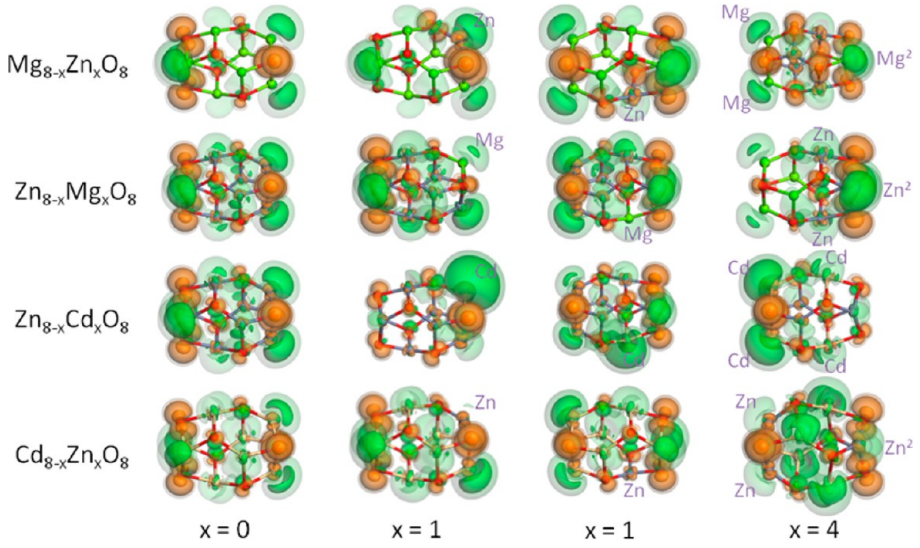

Figure 15. Lowest energy excited electron and hole for $n = 8$ lowest energy (1st and 2nd columns, 1st and 4th row in 4th column), second lowest energy (3rd column), and other (2nd and 3rd row in 4th column) bubble clusters. See caption to Figure 11 for conventions.

behavior of E_g as a function of Mg content from $x = 1$ to $x = 0.625$. At $x = 0.75$ an appreciable scatter of ca. 0.1 eV in E_g values is predicted, which is dependent upon the distance between the two Mg cations. For lower Mg doped rings, E_g increases as the full crown structure emerges. (A constrained planar ring structure has E_g that remains in a continuation of the original constant line at about 4.08 eV.) In these observations, we identify two trends: E_g increases with the degree of corrugation (whch depends on the length of uninterrupted chain(s) of Zn cations) and Mg concentration. Analogously, the uninterrupted chains of Cd dopants dominate the rate of decrease of E_g in Zn:Cd rings. The observed stepwise behavior is in effect an artifact of choosing the line connecting the lowest energy configurations for each stoichiometry of the cluster that minimizes the length of Cd chains. Otherwise, a continuous monotonic decrease should be observed for all major patterns of site occupation.

Turning to more stable structural types, we address first the Mg-rich structures. There is an accidental near degeneracy between the ring and the drum at $x = 1$. On first doping with Zn, E_g has a similar drop both in the drum and bubble series, provided the Zn ion occupies the vertex between two hexagonal and one tetragonal faces rather than between one hexagonal and two tetragonal, which however results in a more stable bubble configuration. The effect on E_g of doping into different (rather than similar) sites is easier to decipher. For example, E_g increases (by a maximum of ~0.1 eV) with distance between zinc cations in the $Zn_2Mg_6O_8$ drums, whereas E_g is smaller (by ~0.05 eV) for $Zn_6Mg_2O_8$ drums if Mg cations reside within the same octagonal ring. The bubble has two unique cation sites, and there is a significant drop in E_g of ~0.3 eV as the first of the four vertices between two hexagonal and one tetragonal faces is doped with Zn. In the series of the lowest energy bubbles (purple curve in Figure 10), this happens at $Zn_5Mg_3O_8$, which is the cause of the noticeable drop. If the electron were to localize primarily on this site, a significant drop in E_g would be related to the initial doping of zinc into the preferred cation site for the electron in both the drum and bubble. However, for the lowest energy exciton in the bubbles (as seen in Figure 15) the electron occupies the other site; hence, it should be the effect the dopant has on the hole that is key to the change in E_g.

In the bubble clusters, the lowest energy exciton is typically composed of a hole in the form of dumbbells on anions, which occupy the vertices between two tetragonal and one hexagonal faces, and an electron localized in an exterior lobe on a number of cations. For Zn:Mg, there are four lobes on cations occupying vertices between two tetragonal and one hexagonal faces. For Zn:Cd the lobes are primarily on the Cd cations that occupy only these sites or alternatively on all Cd cations if these sites are occupied only by Zn. Unlike the cuboid, ring, and bubble structural types, the hole dumbbells on the Zn:Cd $n = 8$ drums are aligned with cation−anion bonds connecting octagonal faces (cf. $n = 6$ drums). The shape of the electron basins is reminiscent of the $n = 4$ and 6 rings, in that there is a appreciable delocalization toward the center of the drum (F center), and of the $n = 6$ drum, in that significant lobes also reside on Cd cations. As the Cd content increases, so does the octagonal ring size and, although still present in the Cd_8O_8 drum, the overlap of the electron lobes within the drum decreases (see Figure 14a−e).

5. SUMMARY AND CONCLUSIONS

In the work presented we focused on the structure and optical properties of Mg and Cd doped ZnO small nanoparticles, or clusters, taking the doping to the limit, i.e., forming the full range of solutions between pure binary phases of these compounds. The key premise has been that we could construct reliable structural models of the clusters from a sufficiently diverse database populated using simple and computationally efficient interatomic potentials. The DFT refinement of the structures considered proved successful—as expected—in that same connectivities and similar energy ranking were obtained. However, we do observe a number of notable rank changes where the energy differences between the local minima are small.

For example, for $n = 4$ we predict the ring structure to be the GM on the IP landscape throughout, whereas on the DFT landscape we find that the cuboid (the first IP metastable structure) is more stable for MgO. On the other hand, for $n = 6$, the reverse is true: IP favors the drum formation throughout whereas DFT suggests that rings (the first IP metastable structure) are more stable for ZnO. As the solution energies we calculate are positive the clusters will disproportionate to the pure binary structures, which could be attributed to the

dx.doi.org/10.1021/jp4084635 | J. Phys. Chem. C 2013, 117, 27127−27145

competition between different structural types adopted by end members. In contrast, the Cd doped systems have negative solution energies and only one dominant structural type.

For n = 8, the largest size considered, the competition for the global minimum of the binary members is between a drum and a bubble, with the two approaches providing different rankings, which is also dependent upon both IP and DFT "flavors" that account with differing accuracy for polarization. On doping, both structures remain close in free energy throughout composition and temperature ranges, which underlines two important conclusions: (i) it is vitally important to include in consideration a number of low-energy minima within a certain range, which could be accessible at least thermally, and (ii) the absolute ranking in an ensemble is not important when the energy differences are small enough to be dependent on the exchange-correlation density functional and/or basis set choice, but must be treated on equal footing, in a "statistical physics" sense.

Considering solutions between two binary compounds, the energy differences between structural types can vary significantly across the range of compositions as seen for Zn:Mg n = 8 series. Therefore, more than one structural type should be considered in practice for any of such solutions, and in this example at least five types from ZnO LM is required in order to obtain the inflated cuboid, which, incidentally, is not found for MgO. The driving force for this rank change between structural types is caused by the inflatable 1 × 1 × 3 cuboid structure having different unique cation sites. The inflated Zn_8O_8 cuboid is stabilized when Mg is doped into the three-coordinated sites, whereas on doping of the two-coordinated sites the structure collapses to the rock-salt analogue. This effect is important at lower temperatures as the site selection penalises the free energy entropic contribution.

Typically, Cd doped three-dimensional clusters absorb in the visible optical range, whereas Mg-rich structures retain their transparency. The generic observation of trends in the band gap behavior of bulk ZnO on doping with isovalent Mg, cations of which have a similar size to Zn^{2+}, and much larger Cd ions are the monotonic blue and red shifts, respectively, which are consistent with the calculated absorption energies for the main structural types of small ZnO clusters discussed in this paper (see Figures 8−10). The notable exceptions generally originate in the structural inhomogeneity of the cluster structures with differently coordinated sites occupied by host or dopant species.

The absorption edge throughout the range of chemical composition and size has an upper bound formed by the ring structural type in agreement with Matxain et al.[32] The gap energy in the rings buck the general trend by not showing a particularly strong dependence on Mg doping and increasing in value with the ring size. In the larger clusters, we observe a structural change in the Zn- and Cd-rich rings, which relax to a crown structure so that on initial Mg doping the expected blue shift is not observed. Drums formed by two parallel rings (tetragons, hexagons, and octagons) form a second set of structural types and follow similar trends found for the rings: a consistent red shift from the Mg-rich end to Cd-rich end via pure ZnO and the value of the gap increasing with size. These observations are contrary to the conventional quantum confinement theory as we have already highlighted previously for a set of high-symmetry bubble structures formed by group 13 nitrides.[64] Indeed, the n = 8 bubble structure investigated here has a similar energy of formation to the n = 8 drum and an analogous optical behavior.

Concerning the localization of hole and electron components of the lowest energy excitons, we find holes typically localize on oxygen lone-pair 2p states, occupying as many anions as possible. For example dumbbell-shaped holes are aligned in parallel to each other and normal to ring planes, but rotate inward in drums and bubbles. As expected, electrons preferentially occupy cations with the highest electronegativity, adjusted by the site coordination and availability. The electron shapes are determined by the shape of single sp^x (x = 1−3) lone pairs, which tend to overlap in ring and drum structures giving rise to F-like centers.

We expect that the trends reported in this study are quite general and transferable to larger sized particles and other 1−1 compounds with a predominantly ionic type of chemical bonding. The predicted absorption edge for the global minima—apart from when there is a change in configuration type—is in qualitative agreement with that observed[9−21] for larger sized particles, i.e., subject to blue and red shifts on doping ZnO with Mg and Cd, respectively, although less monotonic and at a faster rate. Similar trends are found for other metastable configuration types, but now there are notable exceptions. Unsurprisingly, structural types that have more than one symmetry-inequivalent cationic site also display a rate of change that is dependent upon the cation order (and in some examples, the shift is reversed). The opposite trend to that observed for larger particles is also predicted for a number of the metastable structural types: compared to pure ZnO, pure MgO n = 4 chimera, n = 6 H-T-H, and n = 8 ring spectra are red-shifted. Band gap engineering along with similar design driven developments in the field of materials science has resulted in a growing number of reports on synthesis of complex nano-composite materials, which use nanoclusters as building units. The importance of such materials and their design performed at a computational level have been highlighted in refs 66 and 88−90. The range of nano-composite materials could easily be extended by including doped nanoclusters as building units.

AUTHOR INFORMATION

Corresponding Author

*E-mail Scott.Woodley@ucl.ac.uk; Tel +44 (0)20 7679 0315 (S.M.W.).

Notes

The authors declare no competing financial interest.

ACKNOWLEDGMENTS

We thank the British Council, KFUPM and EPSRC (EP/F067496 and EP/I03014X) for support. This work made use of the facilities of HPCx and HECToR, the UK's national high-performance computing service, via our membership of the UK's HPC Materials Chemistry Consortium, which is funded by EPSRC (EP/D504872, EP/F067496 and EP/L000202). We are grateful to Profs Christian Schön, Joseph BelBruno, and Stefan Bromley for useful discussions and encouragement throughout this project.

REFERENCES

(1) Ozgur, U.; Alivov, Y. I.; Liu, C.; Teke, A.; Reshchikov, M. A.; Dogan, S.; Avrutin, V.; Cho, S. J.; Morkoc, H. A Comprehensive Review of ZnO Materials and Devices. *J. Appl. Phys.* **2005**, *98*, 103.

(2) Viswanatha, R.; Sapra, S.; Satpati, B.; Satyam, P. V.; Dev, B. N.; Sarma, D. D. Understanding the Quantum Size Effects in ZnO Nanocrystals. *J. Mater. Chem.* **2004**, *14*, 661−668.

(3) Dallali, L.; Jaziri, S.; El Haskouri, J.; Amorós, P. Optical Properties of Exciton Confinement in Spherical ZnO Quantum Dots Embedded in Matrix. *Superlattices Microstruct.* **2009**, *46*, 907−916.

(4) Antony, J.; Chen, X. B.; Morrison, J.; Bergman, L.; Qiang, Y.; McCready, D. E.; Engelhard, M. H. ZnO Nanoclusters: Synthesis and Photoluminescence. *Appl. Phys. Lett.* **2005**, *87*, 241917.
(5) Schmidt-Mende, L.; MacManus-Driscoll, J. L. ZnO − Nanostructures, Defects, and Devices. *Mater. Today* **2007**, *10*, 40−48.
(6) Catlow, C. R. A.; Bromley, S. T.; Hamad, S.; Mora-Fonz, M.; Sokol, A. A.; Woodley, S. M. Modelling Nano-Clusters and Nucleation. *Phys. Chem. Chem. Phys.* **2010**, *12*, 786−811.
(7) Shannon, R. D. Revised Effective Ionic-Radii and Systematic Studies of Interatomic Distances in Halides and Chalcogenides. *Acta Crystallogr., Sect. A* **1976**, *32*, 751−767.
(8) Catlow, C. R. A.; French, S. A.; Sokol, A. A.; Al-Sunaidi, A. A.; Woodley, S. M. Zinc Oxide: A Case Study in Contemporary Computational Solid State Chemistry. *J. Comput. Chem.* **2008**, *29*, 2234−2249.
(9) Ohtomo, A.; Kawasaki, M.; Koida, T.; Masubuchi, K.; Koinuma, H.; Sakurai, Y.; Yoshida, Y.; Yasuda, T.; Segawa, Y. $Mg_xZn_{1-x}O$ as a II–VI Widegap Semiconductor Alloy. *Appl. Phys. Lett.* **1998**, *72*, 2466.
(10) Ghosh, M.; Raychaudhuri, A. K. Structural and Optical Properties of $Zn_{1-x}Mg_xO$ Nanocrystals Obtained by Low Temperature Method. *J. Appl. Phys.* **2006**, *100*, 034315.
(11) Yadav, M. K.; Ghosh, M.; Biswas, R.; Raychaudhuri, A. K.; Mookerjee, A.; Datta, S. Band-Gap Variation in Mg- and Cd-Doped ZnO Nanostructures and Molecular Clusters. *Phys. Rev. B* **2007**, *76*, 195450.
(12) Ghosh, M.; Raychaudhuri, A. K. Optical Properties of Mg-Substituted ZnO Nanoparticles Obtained by Solution Growth. *IEEE Trans. Nanotechnol.* **2011**, *10*, 555−559.
(13) Chang, Y. S.; Chien, C. T.; Chen, C. W.; Chu, T. Y.; Chiang, H. H.; Ku, C. H.; Wu, J. J.; Lin, C. S.; Chen, L. C.; Chen, K. H. Structural and Optical Properties of Single Crystal $Zn_{1-x}Mg_xO$ Nanorods - Experimental and Theoretical Studies. *J. Appl. Phys.* **2007**, *101*, 033502.
(14) Li, H.; Zhang, Y. Z.; Pan, X. J.; Zhang, H. L.; Wang, T.; Xie, E. Effects of In and Mg Doping on Properties of ZnO Nanoparticles by Flame Spray Synthesis. *J. Nanopart. Res.* **2009**, *11*, 917−921.
(15) Ishihara, J.; Nakamura, A.; Shigemori, S.; Aoki, T.; Temmyo, J. $Zn_{1-x}Cd_xO$ Systems with Visible Band Gaps. *Appl. Phys. Lett.* **2006**, *89*, 091914.
(16) Wang, F. Z.; Ye, Z. Z.; Ma, D. W.; Zhu, L. P.; Zhuge, F.; He, H. P. Synthesis and Characterization of Quasi-Aligned ZnCdO Nanorods. *Appl. Phys. Lett.* **2005**, *87*, 143103.
(17) Wang, Y. S.; Thomas, P. J.; O'Brien, P. Optical Properties of ZnO Nanocrystals Doped with Cd, Mg, Mn, and Fe Ions. *J. Phys. Chem. B* **2006**, *110*, 21412−21415.
(18) Ghosh, M.; Dilawar, N.; Bandyopadhyay, A. K.; Raychaudhuri, A. K. Phonon Dynamics of Zn(Mg,Cd)O Alloy Nanostructures and Their Phase Segregation. *J. Appl. Phys.* **2009**, *106*, 084306.
(19) Maiti, U. N.; Ghosh, P. K.; Ahmed, S. F.; Mitra, M. K.; Chattopadhyay, K. K. Structural, Optical and Photoelectron Spectroscopic Studies of Nano/Micro ZnO: Cd Rods Synthesized Via Sol-Gel Route. *J. Sol-Gel Sci. Technol.* **2007**, *41*, 87−92.
(20) Ghosh, M.; Raychaudhuri, A. K. Structure and Optical Properties of Cd-Substituted ZnO ($Zn_{1-x}Cd_xO$) Nanostructures Synthesized by the High-Pressure Solution Route. *Nanotechnology* **2007**, *18*, 115618.
(21) Wu, S.; Yuan, N.; Xu, H. T.; Wang, X. S.; Schelly, Z. A. Synthesis and Bandgap Oscillation of Uncapped, ZnO Clusters by Electroporation of Vesicles. *Nanotechnology* **2006**, *17*, 4713−4718.
(22) Hammad, T.; Salem, J.; Harrison, R.; Hempelmann, R.; Hejazy, N. Optical and Magnetic Properties of Cu-Doped ZnO Nanoparticles. *J. Mater. Sci.: Mater. Electron* **2013**, *24*, 2846−2852.
(23) Jayakumar, O. D.; Gopalakrishnan, I. K.; Shashikala, K.; Kulshreshtha, S. K.; Sudakar, C. Magnetic Properties of Hydrogenated Li and Co Doped ZnO Nanoparticles. *Appl. Phys. Lett.* **2006**, *89*, 202507.
(24) Oprea, O.; Vasile, O. R.; Voicu, G.; Craciun, L.; Andronescu, E. Photoluminescence, Magnetic Properties and Photocatalytic Activity of Gd^{3+} Doped ZnO Nanoparticles. *Dig. J. Nanomater. Biostruct.* **2012**, *7*, 1757−1766.
(25) Salem, J. K.; Hammad, T. M.; Harrison, R. R. Synthesis, Structural and Optical Properties of Ni-Doped ZnO Micro-Spheres. *J. Mater. Sci.: Mater. Electron.* **2013**, *24*, 1670−1676.
(26) Donkova, B.; Dimitrov, D.; Kostadinov, M.; Mitkova, E.; Mehandjiev, D. Catalytic and Photocatalytic Activity of Lightly Doped Catalysts M:ZnO (M = Cu, Mn). *Mater. Chem. Phys.* **2010**, *123*, 563−568.
(27) Zhao, S. F.; Yao, C. H.; Lu, Q.; Song, F. Q.; Wan, J. G.; Wang, G. H. Cluster-Assembled Cobalt Doped ZnO Nanostructured Film Prepared by Low Energy Cluster Beam Deposition. *Trans. Nonferrous Met. Soc. China* **2009**, *19*, 1450−1453.
(28) Nair, M. G.; Nirmala, M.; Rekha, K.; Anukaliani, A. Structural, Optical, Photo Catalytic and Antibacterial Activity of ZnO and Co Doped ZnO Nanoparticles. *Mater. Lett.* **2011**, *65*, 1797−1800.
(29) Kong, J. Z.; Li, A. D.; Zhai, H. F.; Gong, Y. P.; Li, H.; Wu, D. Preparation, Characterization of the Ta-Doped ZnO Nanoparticles and Their Photocatalytic Activity under Visible-Light Illumination. *J. Solid State Chem.* **2009**, *182*, 2061−2067.
(30) Moafi, H. F.; Zanjanchi, M. A.; Shojaie, A. F. Tungsten-Doped ZnO Nanocomposite: Synthesis, Characterization, and Highly Active Photocatalyst toward Dye Photodegradation. *Mater. Chem. Phys.* **2013**, *139*, 856−864.
(31) Liu, H. L.; Cheng, X.; Liu, H. B.; Yang, J. H.; Liu, Y.; Liu, X. Y.; Gao, M.; Wei, M. B.; Zhang, X.; Jiang, Y. H. Structural, Optical and Magnetic Properties of Cu and V Co-Doped ZnO Nanoparticles. *Phys. E (Amsterdam, Neth.)* **2013**, *47*, 1−5.
(32) Matxain, J. M.; Mercero, J. M.; Fowler, J. E.; Ugalde, J. M. Electronic Excitation Energies of Zn_iO_i Clusters. *J. Am. Chem. Soc.* **2003**, *125*, 9494−9499.
(33) Caddeo, C.; Malloci, G.; De Angelis, F.; Colombo, L.; Mattoni, A. Optoelectronic Properties of $(ZnO)_{60}$ Isomers. *Phys. Chem. Chem. Phys.* **2012**, *14*, 14293−14298.
(34) Gunaratne, K. D. D.; Berkdemir, C.; Harmon, C. L.; Castleman, A. W. Investigating the Relative Stabilities and Electronic Properties of Small Zinc Oxide Clusters. *J. Phys. Chem. A* **2012**, *116*, 12429−12437.
(35) Sarsari, I. A.; Hashemifar, S. J.; Salamati, H. First-Principles Study of Ring to Cage Structural Crossover in Small ZnO Clusters. *J. Phys.: Condens. Matter* **2012**, *24*, 505502.
(36) Azpiroz, J. M.; Mosconi, E.; De Angelis, F. Modeling ZnS and ZnO Nanostructures: Structural, Electronic, and Optical Properties. *J. Phys. Chem. C* **2011**, *115*, 25219−25226.
(37) Malloci, G.; Chiodo, L.; Rubio, A.; Mattoni, A. Structural and Optoelectronic Properties of Unsaturated ZnO and ZnS Nanoclusters. *J. Phys. Chem. C* **2012**, *116*, 8741−8746.
(38) Haertelt, M.; Fielicke, A.; Meijer, G.; Kwapien, K.; Sierka, M.; Sauer, J. Structure Determination of Neutral MgO Clusters-Hexagonal Nanotubes and Cages. *Phys. Chem. Chem. Phys.* **2012**, *14*, 2849−2856.
(39) Srinivasaraghavan, R.; Chandiramouli, R.; Jeyaprakash, B. G.; Seshadri, S. Quantum Chemical Studies on CdO Nanoclusters Stability. *Spectrochim. Acta, Part A* **2013**, *102*, 242−249.
(40) Wang, C. L.; Xu, S. H.; Ye, L. H.; Lei, W.; Cui, Y. P. Theoretical Investigation of ZnO and Its Doping Clusters. *J. Mol. Model.* **2011**, *17*, 1075−1080.
(41) Ahmad Siddiqui, S.; Abdullah, M. M. Quantum Chemical Study of Fe Doped ZnO Nanoclusters. *Micro Nanosyst.* **2013**, *5*, 14−21.
(42) Badaeva, E.; Feng, Y.; Gamelin, D. R.; Li, X. S. Investigation of Pure and Co^{2+}-Doped ZnO Quantum Dot Electronic Structures Using the Density Functional Theory: Choosing the Right Functional. *New J. Phys.* **2008**, *10*, 055013.
(43) Yong, Y. L.; Wang, Z.; Liu, K.; Song, B.; He, P. M. Structures, Stabilities, and Magnetic Properties of Cu-Doped Zn_nO_n (n=3,9,12) Clusters: A Theoretical Study. *Comput. Theor. Chem.* **2012**, *989*, 90−96.
(44) Nanavati, S. P.; Sundararajan, V.; Mahamuni, S.; Ghaisas, S. V.; Kumar, V. Nonstoichiometric Mn-Doped ZnO Magic Nanoclusters and Their Composite Structures from Ab Initio Calculations. *Phys. Rev. B* **2012**, *86*, 205320.
(45) Chen, Q.; Wang, J. L. Structural, Electronic, and Magnetic Properties of $TMZn_{11}O_{12}$ and $TM_2Zn_{10}O_{12}$ Clusters (TM = Sc, Ti, V, Cr, Mn, Fe, Co, Ni, and Cu). *Chem. Phys. Lett.* **2009**, *474*, 336−341.

(46) Ganguli, N.; Dasgupta, I.; Sanyal, B. Electronic Structure and Magnetism of Transition Metal Doped $Zn_{12}O_{12}$ Clusters: Role of Defects. *J. Appl. Phys.* **2010**, *108*, 123911.
(47) Ganguli, N.; Dasgupta, I.; Sanyal, B. The Making of Ferromagnetic Fe Doped ZnO Nanoclusters. *Appl. Phys. Lett.* **2009**, *94*, 192503.
(48) Ovsiannikova, L. Model and Properties of Fullerene-Like and Wurtzite-Like ZnO and Zn(Cd)O Clusters. *Acta Phys. Pol., A* **2012**, *122*, 1062−1064.
(49) Wang, Q. J.; Wang, J. B.; Zhong, X. L.; Tan, Q. H.; Zhou, Y. C. Magnetic Properties of C-Doped $Zn_{12}O_{12}$ Clusters: First-Principles Study. *EPL* **2011**, *95*, 47010.
(50) Nagare, B. J.; Chacko, S.; Kanhere, D. G. Ferromagnetism in Carbon-Doped Zinc Oxide Systems. *J. Phys. Chem. A* **2010**, *114*, 2689−2696.
(51) Sharma, H.; Singh, R. Spin-Polarized Density Functional Investigation into Ferromagnetism in C-Doped $(ZnO)_n$ Clusters; n=1−12, 16. *J. Phys.: Condens. Matter* **2011**, *23*, 106004.
(52) Botello-Mendez, A. R.; Lopez-Urias, F.; Terrones, M.; Terrones, H. Effect of Impurities on the Electronic and Magnetic Properties of Zinc Oxide Nanostructures. *Chem. Phys. Lett.* **2010**, *492*, 82−88.
(53) Kapila, N.; Jindal, V. K.; Sharma, H. The Role of N Dopant in Inducing Ferromagnetism in $(ZnO)_n$ Clusters (n=1−16). *J. Phys.: Condens. Matter* **2011**, *23*, 446006.
(54) Yong, Y. L.; Song, B.; He, P. M. Density-Functional Study of Structural, Electronic, and Magnetic Properties of N-Doped Zn_nO_n (n=2−13) Clusters. *Comput. Theor. Chem.* **2013**, *1012*, 14−19.
(55) Flores-Hidalgo, M. A.; Barraza-Jimenez, D.; Glossman-Mitnik, D. Effects of Sulfur Substitutional Impurities on $(ZnO)_n$ Clusters (n=4−12) Using Density Functional Theory. *Comput. Theor. Chem.* **2011**, *965*, 154−162.
(56) Hidalgo, M. A. F.; Jimenez, D. B.; Glossman-Mitnik, D. Excited States Analysis of Sulfur Substitutional Impurities on $(ZnO)_6$ Clusters Using DFT and TD-DFT. *J. Mol. Struct.: THEOCHEM* **2010**, *957*, 100−107.
(57) Amat, A.; De Angelis, F. Challenges in the Simulation of Dye-Sensitized ZnO Solar Cells: Quantum Confinement, Alignment of Energy Levels and Excited State Nature at the Dye/Semiconductor Interface. *Phys. Chem. Chem. Phys.* **2012**, *14*, 10662−10668.
(58) Azpiroz, J. M.; Infante, I.; Lopez, X.; Ugalde, J. M.; De Angelis, F. A First-Principles Study of II-VI (II = Zn; VI = O, S, Se, Te) Semiconductor Nanostructures. *J. Mater. Chem.* **2012**, *22*, 21453−21465.
(59) De Angelis, F.; Armelao, L. Optical Properties of ZnO Nanostructures: A Hybrid DFT/TDDFT Investigation. *Phys. Chem. Chem. Phys.* **2011**, *13*, 467−475.
(60) Saha, S.; Sarkar, S.; Pal, S.; Sarkar, P. Ligand Mediated Tuning of the Electronic Energy Levels of ZnO Nanoparticles. *RSC Adv.* **2013**, *3*, 532−539.
(61) Woodley, S. M.; Sokol, A. A.; Catlow, C. R. A. Structure Prediction of Inorganic Nanoparticles with Predefined Architecture Using a Genetic Algorithm. *Z. Anorg. Allg. Chem.* **2004**, *630*, 2343−2353.
(62) Hamad, S.; Catlow, C. R. A.; Woodley, S. M.; Lago, S.; Mejias, J. A. Structure and Stability of Small TiO_2 Nanoparticles. *J. Phys. Chem. B* **2005**, *109*, 15741−15748.
(63) Woodley, S. M.; Hamad, S.; Mejias, J. A.; Catlow, C. R. A. Properties of Small TiO_2, ZrO_2 and HfO_2 Nanoparticles. *J. Mater. Chem.* **2006**, *16*, 1927−1933.
(64) Shevlin, S. A.; Guo, Z. X.; van Dam, H. J. J.; Sherwood, P.; Catlow, C. R. A.; Sokol, A. A.; Woodley, S. M. Structure, Optical Properties and Defects in Nitride (III-V) Nanoscale Cage Clusters. *Phys. Chem. Chem. Phys.* **2008**, *10*, 1944−1959.
(65) Al-Sunaidi, A. A.; Sokol, A. A.; Catlow, C. R. A.; Woodley, S. M. Structures of Zinc Oxide Nanoclusters: As Found by Evolutionary Algorithm Techniques. *J. Phys. Chem. C* **2008**, *112*, 18860−18875.
(66) Watkins, M. B.; Shevlin, S. A.; Sokol, A. A.; Slater, B.; Catlow, C. R. A.; Woodley, S. M. Bubbles and Microporous Frameworks of Silicon Carbide. *Phys. Chem. Chem. Phys.* **2009**, *11*, 3186−3200.
(67) Woodley, S. M.; Hamad, S.; Catlow, C. R. A. Exploration of Multiple Energy Landscapes for Zirconia Nanoclusters. *Phys. Chem. Chem. Phys.* **2010**, *12*, 8454−8465.
(68) Walsh, A.; Woodley, S. M. Evolutionary Structure Prediction and Electronic Properties of Indium Oxide Nanoclusters. *Phys. Chem. Chem. Phys.* **2010**, *12*, 8446−8453.
(69) Sokol, A. A.; Catlow, C. R. A.; Miskufova, M.; Shevlin, S. A.; Al-Sunaidi, A. A.; Walsh, A.; Woodley, S. M. On the Problem of Cluster Structure Diversity and the Value of Data Mining. *Phys. Chem. Chem. Phys.* **2010**, *12*, 8438−8445.
(70) Woodley, S. M. Atomistic and Electronic Structure of $(X_2O_3)_n$ Nanoclusters; n=1−5, X = B, Al, Ga, In and Tl. *Proc. R. Soc. A: Math. Phys. Eng. Sci.* **2011**, *467*, 2020−2042.
(71) Shevlin, S. A.; Woodley, S. M. Electronic and Optical Properties of Doped and Undoped $(TiO_2)_n$ Nanoparticles. *J. Phys. Chem. C* **2010**, *114*, 17333−17343.
(72) Woodley, S. M. Structure Prediction of Ternary Oxide Sub-Nanoparticles. *Mater. Manuf. Processes* **2009**, *24*, 255−264.
(73) Heiles, S.; Johnston, R. L. Global Optimization of Clusters Using Electronic Structure Methods. *Int. J. Quantum Chem.* **2013**, *113*, 2091−2109.
(74) Sierka, M.; Dobler, J.; Sauer, J.; Santambrogio, G.; Brummer, M.; Woste, L.; Janssens, E.; Meijer, G.; Asmis, K. R. Unexpected Structures of Aluminum Oxide Clusters in the Gas Phase. *Angew. Chem., Int. Ed.* **2007**, *46*, 3372−3375.
(75) Woodley, S. M.; Battle, P. D.; Gale, J. D.; Catlow, C. R. A. The Prediction of Inorganic Crystal Structures Using a Genetic Algorithm and Energy Minimisation. *Phys. Chem. Chem. Phys.* **1999**, *1*, 2535−2542.
(76) Whitmore, L.; Sokol, A. A.; Catlow, C. R. A. Surface Structure of Zinc Oxide (1010), Using an Atomistic, Semi-Infinite Treatment. *Surf. Sci.* **2002**, *498*, 135−146.
(77) Delley, B. From Molecules to Solids with the Dmol(3) Approach. *J. Chem. Phys.* **2000**, *113*, 7756−7764.
(78) Delley, B. An All-Electron Numerical-Method for Solving the Local Density Functional for Polyatomic-Molecules. *J. Chem. Phys.* **1990**, *92*, 508−517.
(79) Perdew, J. P.; Burke, K.; Ernzerhof, M. Generalized Gradient Approximation Made Simple. *Phys. Rev. Lett.* **1996**, *77*, 3865.
(80) Purton, J. A.; Allan, N. L.; Lavrentiev, M. Y.; Todorov, I. T.; Freeman, C. L. Computer Simulation of Mineral Solid Solutions. *Chem. Geol.* **2006**, *225*, 176−188.
(81) Roberts, C.; Johnston, R. L. Investigation of the Structures of MgO Clusters Using a Genetic Algorithm. *Phys. Chem. Chem. Phys.* **2001**, *3*, 5024−5034.
(82) Valiev, M.; Bylaska, E. J.; Govind, N.; Kowalski, K.; Straatsma, T. P.; Van Dam, H. J. J.; Wang, D.; Nieplocha, J.; Apra, E.; Windus, T. L.; de Jong, W. NWChem: A Comprehensive and Scalable Open-Source Solution for Large Scale Molecular Simulations. *Comput. Phys. Commun.* **2010**, *181*, 1477−1489.
(83) Adamo, C.; Barone, V. Toward Reliable Density Functional Methods without Adjustable Parameters: The PBE0Model. *J. Chem. Phys.* **1999**, *110*, 6158−6170.
(84) Casida, M. E.; Jamorski, C.; Casida, K. C.; Salahub, D. R. Molecular Excitation Energies to High-Lying Bound States from Time-Dependent Density-Functional Response Theory: Characterization and Correction of the Time-Dependent Local Density Approximation Ionization Threshold. *J. Chem. Phys.* **1998**, *108*, 4439−4449.
(85) Zhan, C. G.; Nichols, J. A.; Dixon, D. A. Ionization Potential, Electron Affinity, Electronegativity, Hardness, and Electron Excitation Energy: Molecular Properties from Density Functional Theory Orbital Energies. *J. Phys. Chem. A* **2003**, *107*, 4184−4195.
(86) Kaupp, M.; Schleyer, P. V.; Stoll, H.; Preuss, H. Pseudopotential Approaches to Ca, Sr, and Ba Hybrides - Why Are Some Alkaline-Earth MX_2 Compounds Bent. *J. Chem. Phys.* **1991**, *94*, 1360−1366.
(87) Figgen, D.; Rauhut, G.; Dolg, M.; Stoll, H. Energy-Consistent Pseudopotentials for Group 11 and 12 Atoms: Adjustment to Multi-Configuration Dirac-Hartree-Fock Data. *Chem. Phys.* **2005**, *311*, 227−244.

(88) Carrasco, J.; Illas, F.; Bromley, S. T. Ultralow-Density Nanocage-Based Metal-Oxide Polymorphs. *Phys. Rev. Lett.* **2007**, *99*, 235502e.
(89) Woodley, S. M.; Watkins, M. B.; Sokol, A. A.; Shevlin, S. A.; Catlow, C. R. A. Construction of Nano- and Microporous Frameworks from Octahedral Bubble Clusters. *Phys. Chem. Chem. Phys.* **2009**, *11*, 3176−3185.
(90) Liu, Z.; Wang, X.; Cai, J.; Liu, G.; Zhou, P.; Wang, K.; Zhu, H. From the ZnO Hollow Cage Clusters to ZnO Nanoporous Phases: A First-Principles Bottom-up Prediction. *J. Phys. Chem. C* **2013**, *117*, 17633−17643.